

# Revisiting the Austral Spring Extratropical Southern Hemisphere zonally asymmetric circulation using complex Empirical Orthogonal Functions

Elio Campitelli<sup>1,2,3\*</sup>, Leandro B. Díaz<sup>1,2,3</sup> and Carolina  
Vera<sup>1,2,3</sup>

<sup>1</sup>\*Universidad de Buenos Aires, Facultad de Ciencias Exactas y  
Naturales, Departamento de Ciencias de la Atmósfera y los  
Océanos, Buenos Aires, Argentina.

<sup>2</sup>\*CONICET – Universidad de Buenos Aires. Centro de  
Investigaciones del Mar y la Atmósfera (CIMA), Buenos Aires,  
Argentina.

<sup>3</sup>CNRS – IRD – CONICET – UBA. Instituto Franco-Argentino  
para el Estudio del Clima y sus Impactos (IRL 3351 IFAECI),  
Buenos Aires, Argentina.

\*Corresponding author(s). E-mail(s):  
[elio.campitelli@cima.fcen.uba.ar](mailto:elio.campitelli@cima.fcen.uba.ar);

## Abstract

The large-scale extratropical circulation in the Southern Hemisphere is much more zonally symmetric than that of the Northern Hemisphere, but its zonal departures, albeit highly relevant for regional impacts, have been less studied. In this study we analyse the joint variability of the zonally asymmetric springtime stratospheric and tropospheric circulation using Complex Empirical Orthogonal Functions (cEOF) to characterise planetary waves of varying amplitude and phase. The leading cEOF represents variability of a zonal wave 1 in the stratosphere that correlates slightly with the Symmetric Southern Annular Mode (S-SAM). The second cEOF (cEOF2) is an alternative representation of the Pacific-South American modes. One phase of this cEOF is also extremely correlated with the Asymmetric SAM (A-SAM)

## 2 SH zonally asymmetric circulation with cEOF

047 in the troposphere. Springs with an active ENSO tend to phase-lock  
 048 the cEOF2, but have no consistent impact on its magnitude. Fur-  
 049 thermore, we find indications that the location of Pacific Sea Surface  
 050 Temperature anomalies affect the phase of the cEOF2. As a result, the  
 051 methodology proposed in this study provides a deeper understanding  
 052 of the zonally asymmetric springtime extratropical SH circulation.

053 **Keywords:** Southern Hemisphere circulation, Teleconnections, Pacific South  
 054 American Mode, Southern Annular Mode, Stratosphere

## 058 1 Introduction

### introduction

060 The large-scale extratropical circulation in the Southern Hemisphere (SH) is  
 061 much more zonally symmetric than that of the Northern Hemisphere, but  
 062 departures from the zonal mean are associated with regional impacts (e.g.  
 063 [Hoskins and Hedges, 2005](#)). They strongly modulate weather systems and  
 064 regional climate through promoting longitudinally varying meridional trans-  
 065 port of heat, humidity, and momentum ([Trenberth, 1980](#); [Raphael, 2007](#)) and  
 066 could even be related to the occurrence of high-impact climate extremes ([Pezza](#)  
 067 [et al, 2012](#)).

068 The zonally asymmetric circulation is typically described by the amplitude  
 069 and phase of zonal waves obtained by Fourier decomposition of geopotential  
 070 height or sea-level pressure at each latitude (e.g. [van Loon and Jenne, 1972](#);  
 071 [Trenberth, 1980](#); [Turner et al, 2017](#)). This approach suggests that zonal waves  
 072 1 and 3 explain almost 99% of the total variance in the annual mean 500 hPa  
 073 geopotential height zonal anomalies at 50°S ([van Loon and Jenne, 1972](#)). [Tren-](#)  
 074 [berth and Mo \(1985\)](#) concluded that wave 3 plays a role in the development  
 075 of blocking events. In addition, previous works have identified wave-like pat-  
 076 terns with dominant wavenumbers 3-4 at extratropical and subpolar latitudes  
 077 with distinctive regional impacts. [Raphael \(2007\)](#) showed that variability in  
 078 the planetary wave 3 projected onto its climatological location is associated  
 079 with anomalies in the Antarctic sea-ice concentration.

080 Fourier decomposition relies on the assumption that the circulation can be  
 081 meaningfully described in terms of zonal waves of constant amplitude along a  
 082 latitude circle. However, this is not valid for meridionally propagating waves or  
 083 zonal waves with localised amplitudes. Addressing this limitation, the Fourier  
 084 technique can be generalized to integrate all planetary wave amplitude regard-  
 085 less of wave number by computing the wave envelope ([Irving and Simmonds,](#)  
 086 [2015](#)). The wave envelope can represent planetary waves with different ampli-  
 087 tude at different longitudes, but lacks information about phase and wave  
 088 number. Using this method, [Irving and Simmonds \(2015\)](#) showed that plane-  
 089 tary wave amplitude in general is associated to Antarctic sea-ice concentration  
 090 and temperature, as well as to precipitation anomalies in regions of significant  
 091 topography in SH mid-latitudes and Antarctica.

Another extensively-used approach to characterise the SH tropospheric circulation anomalies, is computing Empirical Orthogonal Functions (EOF, also known as Principal Component Analysis). Within the EOF framework, the Southern Annular Mode (SAM) appears as the leading mode of variability of the SH circulation (Fogt and Marshall, 2020). The SAM represents a relatively zonally symmetric pattern of alternating low pressures in polar latitudes and a ring of high pressures in high latitudes with an embedded wave 3 pattern that is more prominent in the Pacific sector. The 2nd and 3rd EOFs, usually known as Pacific–South American Patterns (PSA) 1 and PSA2 patterns, respectively, describe meridionally propagating wave trains that originate in the eastern equatorial Pacific and Australian-Indian Ocean sector, and travel towards the South Atlantic following a great-circle arch along the Antarctic coast (Mo and Paegle, 2001). These patterns influence precipitation anomalies in South America (Mo and Paegle, 2001). Although these patterns are usually derived by applying EOF to temporal anomalies, Raphael (2003) also applied EOF methods specifically to zonal anomalies. Irving and Simmonds (2016) proposed a novel methodology for objectively identifying the PSA pattern using Fourier decomposition. More recently Goyal et al (2022) created an index of amplitude and phase of zonal wave 3-like variability by combining the two leading EOFs of meridional wind anomalies.

Some of the zonally asymmetric patterns of the SH circulation variability described previously appear to have experienced secular changes. For instance, Raphael (2003) suggests that the amplitude of the zonal wave 1 experienced a large increase and that the zonal wave 3 experienced changes in its annual cycle between 1958 and 1996. However, little is known yet about variability and trends of these patterns.

Patterns resulting from EOF analysis are more flexible than Fourier decomposition-derived modes in that they can capture oscillation patterns that cannot be characterised by purely sinusoidal waves with constant amplitude. Nonetheless, they are restricted to standing oscillation modes and cannot properly represent propagating or phase-varying features such as zonal waves. A single EOF can also represent a mixture of two or more physical modes.

A third methodology commonly used to describe circulation anomalies consists on identifying particular features of interest and creating indices using simple methods such as averages and differences. Examples of this methodology are the SAM Index of Gong and Wang (1999), the SH wave 3 activity index defined by Raphael (2004) and the SH zonally asymmetric circulation index from Hobbs and Raphael (2010). These derived methods are grounded on other methods such as Fourier decomposition or EOF to identify the centres of action for the described phenomena and can be useful to characterise features that are not readily apparent with these methods. These kinds of indices are generally easy to compute, but they usually do not capture non-stationary patterns.

An alternative methodology that has been proposed to study travelling and standing waves is complex Empirical Orthogonal Functions (cEOF; Horel

#### 4 SH zonally asymmetric circulation with cEOF

139 (1984)). This method extends EOF analysis to capture oscillations with vary-  
 140 ing amplitude and phase and has been applied to the time domain. For  
 141 instance, Krokkin and Luxemburg (2007) applied cEOF to station-based  
 142 monthly precipitation anomalies and monthly temperature anomalies in the  
 143 Eastern Siberia and the Far East region to characterise the main modes of vari-  
 144 ability and their relationship with teleconnection indices. Similarly, Gelbrecht  
 145 et al (2018) applied cEOF to daily precipitation from reanalysis to study the  
 146 propagating characteristics of the South American Monsoon. To our knowl-  
 147 edge, cEOF analysis has not been applied in the spatial domain to capture  
 148 the phase-varying nature of planetary waves in the atmosphere.

149 The general goal of this study is to improve the description and under-  
 150 standing of the zonally asymmetric extratropical SH circulation using cEOF,  
 151 which can describe phase varying planetary waves with variable amplitude  
 152 along a latitude circle. In addition, we try to expand the knowledge of the  
 153 simultaneous behaviour of SH asymmetric circulation in the troposphere and  
 154 the stratosphere.

155 We restrict this work to the September-October-November (SON)  
 156 trimester because during this season both the tropical teleconnections  
 157 over South America (Cazes-Boezio et al, 2003) and the SH stratosphere-  
 158 troposphere interactions (Lim et al, 2018) are at their maximum amplitude.

159 In Section 2 we describe the methods. In Section 3.1 we analyse the spatial  
 160 patterns of each complex EOF. In Section 3.2 we study the spatial regressions  
 161 with geopotential height, temperature and ozone anomalies. In Section 3.3 and  
 162 3.4 we analyse the relationship between cEOF2, the PSA and SAM modes. In  
 163 Section 3.5 we study tropical forcings that explain the variability of each cEOF.  
 164 In Section 3.6 we show the relationship between these modes of variability  
 165 and precipitation and surface temperature anomalies in South America and  
 166 Oceania. In Section 4 we compare our results with previous studies and discuss  
 167 the benefits of our methodology.

168

## 169 2 Data and Methods

170

### 171 2.1 Data

172

173 We used monthly geopotential height, air temperature, ozone mixing ratio,  
 174 and total column ozone (TOC) at 2.5° longitude by 2.5° latitude of hori-  
 175 zontal resolution and 37 vertical isobaric levels from the European Centre for  
 176 Medium-Range Weather Forecasts Reanalysis version 5 [ERA; Hersbach et al  
 177 (2019)] for the period 1979 – 2019. Most of our analysis is restricted to the  
 178 post-satellite era to avoid confounding factors arising from the incorporation  
 179 of satellite observations, but we also used the preliminary back extension of  
 180 ERA5 from 1950 to 1978 (Bell et al, 2020) to describe long-term trends. We  
 181 derived streamfunction at 200 hPa from ERA5 vorticity using the FORTRAN  
 182 subroutine FISHPACK (Adams et al, 1999) and we computed horizontal  
 183 wave activity fluxes following Plumb (1985). Sea Surface Temperature (SST)  
 184 monthly fields are from Extended Reconstructed Sea Surface Temperature

methods

data

(ERSST) v5 (Huang et al, 2017) and precipitation monthly data from the CPC Merged Analysis of Precipitation (CMAP, Xie and Arkin, 1997), with a  $2^{\circ}$  and  $2.5^{\circ}$  horizontal resolution, respectively. The rainfall gridded dataset is based on information from different sources such as rain gauge observations, satellite inferred estimations and the NCEP-NCAR reanalysis, and it is available from 1979 to the present.

The Oceanic Niño Index (ONI, Bamston et al, 1997) comes from NOAA's Climate Prediction Center and the Dipole Mode Index (DMI, Saji and Yamagata, 2003) from Global Climate Observing System Working Group on Surface Pressure.

## 2.2 Methods

The study is restricted to the spring season, defined as the September-October-November (SON) trimester. We compute seasonal means for the different variables, averaging monthly values weighted by the number of days in each month. We use the 200 hPa level to represent the high troposphere and 50 hPa to represent the lower stratosphere.

We computed the amplitude and phase of the TOC wave 1 by averaging (area-weighted) the data of each SON between  $75^{\circ}$ S and  $45^{\circ}$ S, and then extracting the wave-1 component of the Fourier spectrum. We chose this latitude band because it is wide enough to capture most of the relevant anomalies of SH mid-latitudes.

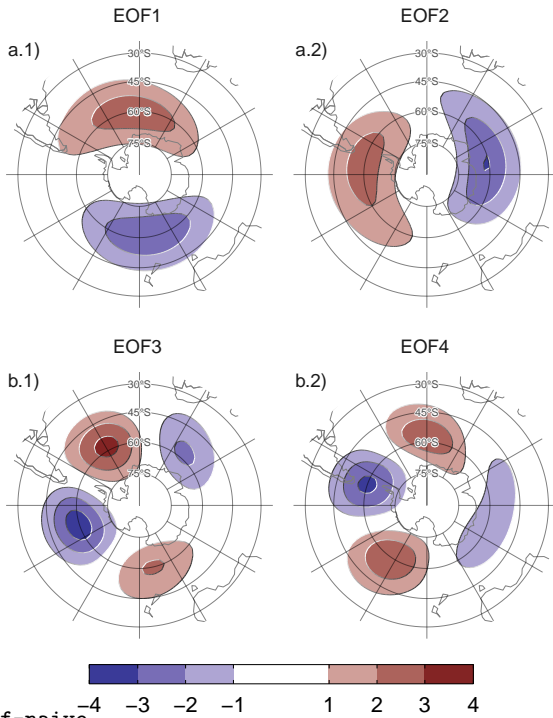
We computed the level-dependent SAM index as the leading EOF of year-round monthly geopotential height anomalies south of  $20^{\circ}$ S at each level for the whole period (Baldwin and Thompson, 2009). We further split the SAM into its zonally symmetric and zonally asymmetric components (S-SAM and A-SAM indices respectively). These indices were obtained by projecting monthly geopotential height fields onto the zonally asymmetric and zonally symmetric parts of the SAM spatial pattern, as proposed by Campitelli et al (2022b). Seasonal indices of the PSA patterns (PSA1 and PSA2) were calculated, in agreement with Mo and Paegle (2001), as the third and fourth EOFs of seasonal mean anomalies for 500-hPa geopotential heights at SH.

Linear trends were computed by Ordinary Least Squares (OLS) and the 95% confidence interval was computed assuming a t-distribution with the appropriate residual degrees of freedom (Wilks, 2011).

## 2.3 Complex Empirical Orthogonal Functions (cEOF)

In the standard EOF analysis, zonal waves may appear as pairs of (possibly degenerate) EOFs representing similar patterns but shifted in phase (Horel, 1984). Figure 1 shows the four leading EOFs of SON geopotential height zonal anomalies at 50 hPa south of  $20^{\circ}$  S. It is clear that the first two EOFs represent a single phase-varying zonal wave 1 pattern and the last two represent a similarly phase-varying pattern with higher wavenumber and three centres of action shifted by  $1/4$  wavelength ( $90^{\circ}$  in frequency space).

	185
	186
	187
	188
	189
	190
	191
	192
	193
	194
	195
methods-1	196
	197
	198
	199
	200
	201
	202
	203
	204
	205
	206
	207
	208
	209
	210
	211
	212
	213
	214
	215
	216
	217
	218
	219
	220
	221
	222
	223
	224
	225
	226
	227
	228
	229
	230

6 *SH zonally asymmetric circulation with cEOF*231  
232  
233  
234  
235  
236  
237  
238  
239  
240

251  
252 **Fig. 1:** Spatial patterns of the four leading EOFs of SON geopotential height  
253 zonal anomalies at 50 hPa south of 20° S for the 1979 – 2019 period (arbitrary  
254 units).  
255

256  
257

258 To describe the phase-varying nature of these two wave patterns, one way  
259 is to combine each pair of EOFs into indices of amplitude and phase. So,  
260 for instance, the amplitude of the wave 1-like EOF could be measured as  
261  $\sqrt{PC1^2 + PC2^2}$  and its phase as  $\tan^{-1}(\frac{PC2}{PC1})$  (where PC1 and PC2 are the  
262 time series associated with each EOF). However, this rests on visual inspection  
263 of the spatial patterns and only works properly if both phases appear clearly  
264 in different EOFs, which is not guaranteed by construction. In particular, this  
265 does not work with the wave 1 pattern depicted as the leading EOF in 200  
266 hPa geopotential height zonal anomalies (not shown).  
267

268 On the other hand, a better alternative for describing phase-varying waves  
269 is to use Complex Empirical Orthogonal Functions (cEOF) analysis (Horel,  
270 1984). Each cEOF is a set of complex-valued spatial patterns and time series.  
271 The real and imaginary components of the complex spatial pattern can be  
272 thought of as representing two spatial patterns that are shifted by 1/4 wave-  
273 length by construction, similar to EOF1 and EOF2 in Figure 1. In this paper  
274 we use the term 0° cEOF and 90° cEOF to refer to each part of the whole  
275 cEOF. The actual field reconstructed by each cEOF is then the linear combi-  
276 nation of the two spatial fields weighted by its respective time series. This

**Table 1:** tab:corr-ceof-splitted Coefficient of determination ( $r^2$ ) between the time series of the absolute magnitude of complex EOFs computed separately at 200 hPa and 50 hPa (p-values lower than 0.01 in bold).

		50 hPa		
		cEOF1	cEOF2	cEOF3
200 hPa				
cEOF1	<b>0.29</b>	0.01	0.03	
cEOF2	0.00	<b>0.59</b>	0.02	
cEOF3	0.00	0.00	0.01	

is analogous to how any sine wave can be constructed by the sum of a sine wave and cosine wave with different amplitude but constant phase. This means that cEOFs naturally represent phase-varying wave-like patterns that change location as well as amplitude.

For instance, when the phase of the wave matches the  $0^\circ$  phase, then the  $0^\circ$  phase time series is positive and the  $90^\circ$  phase time series is zero. Similarly, when the phase of the wave matches the  $90^\circ$  phase, the  $90^\circ$  phase time series is positive and the  $0^\circ$  phase time series is zero. The intermediate phases have non-zero values in both time series.

Traditional EOFs are not unique, and instead are defined up to sign, which corresponds to a rotation in the complex plane of either 0 or  $\pi$ . In the same way, cEOFs are defined up to a rotation in the complex plane of any value between 0 and  $2\pi$  (Horel, 1984).

cEOFs are computed in the same way as traditional EOFs except that the data is first augmented by computing its analytic signal. This is a complex number whose real part is the original series and whose imaginary part is the original data shifted by  $90^\circ$  at each spectral frequency – i.e. its Hilbert transform. The Hilbert transform is usually understood in terms of time-varying signal. However, in this work we apply the Hilbert transform at each latitude circle and at each considered time (i.e. the signal only depends on longitude). Since each latitude circle is a periodic domain, this procedure does not suffer from edge effects.

We first applied cEOF analysis to geopotential height zonal anomalies south of  $20^\circ\text{S}$  at 50 and at 200 hPa. Figure 2 a.1 shows the spatial patterns of the two leading cEOF. The  $0^\circ$  phase is plotted with shaded contours and the  $90^\circ$  phase, with black contours. The two phases of the leading cEOF are very similar to the two leading EOFs shown in Figure 1 and represent a zonal wave 1 pattern; the  $0^\circ$  phase is roughly the EOF1 and the  $90^\circ$  phase is roughly the EOF2).

Table 1 shows the coefficient of determination between time series of the amplitude of each cEOF across levels. There is a high degree of correlation between the magnitude of the respective cEOF1 and cEOF2 at each level. The spatial patterns of the 50 hPa and 200 hPa cEOFs are also similar (not shown).

8 *SH zonally asymmetric circulation with cEOF*

323 Both the spatial pattern similarity and the high temporal correlation of  
 324 cEOFs computed at 50 hPa and 200 hPa suggest that these are, to a large  
 325 extent, modes of joint variability. This motivates the decision of performing  
 326 cEOF jointly between levels. Therefore cEOFs were computed using data from  
 327 both levels at the same time. In that sense each cEOF has a spatial component  
 328 that depends on longitude, latitude and level, and a temporal component that  
 329 depends only on time.

330 As mentioned before, the choice of phases is arbitrary and equally valid.  
 331 But to make the interpretation easier, we chose the phase of each cEOF so  
 332 that either the 0° cEOF or the 90° cEOF is aligned with meaningful variables  
 333 in our analysis. This procedure does not create spurious correlations, it only  
 334 takes an existing relationship and aligns it with a specific phase.

335 Preliminary analysis showed that the first cEOF was closely related to the  
 336 zonal wave 1 of TOC and the second cEOF was closely related to ENSO.  
 337 Therefore, we chose the phase of cEOF1 so that the time series corresponding  
 338 to the 0° cEOF1 has the maximum correlation with the zonal wave 1 of TOC  
 339 between 75°S and 45°S. Similarly, we chose the phase of cEOF2 so that the  
 340 coefficient of determination between the ONI and the 0° cEOF2 is minimised,  
 341 which also nearly maximises the correlation with the 90° cEOF2.

342 In Section 3.6 we show regressions of precipitation and temperature associated  
 343 with intermediate phases. For those plots, we rotated the cEOFs by 1/4  
 344 wavelength by multiplying the complex time series by  $\cos(\pi/4) + i \sin(\pi/4)$   
 345 and computing the regression on those rotated timeseries.

346 While we compute these complex principal components using data from  
 347 1979 to 2019, we extended the complex time series back to the 1950 – 1978  
 348 period by projecting monthly geopotential height zonal anomalies standardised  
 349 by level south of 20°S onto the corresponding spatial patterns.

350 We performed linear regressions to quantify the association between the  
 351 cEOFs and other variables (e.g. geopotential height, temperature, precipitation,  
 352 and others). For each cEOF, we computed regression maps by fitting a  
 353 multiple linear model involving both the 0° and the 90° phases. To obtain the  
 354 linear coefficients of a variable  $X$  with the 0° and 90° phase of each cEOF we  
 355 fit the equation

356

357

$$358 X(\lambda, \phi, t) = \alpha(\lambda, \phi) \text{cEOF}_0 + \beta(\lambda, \phi) \text{cEOF}_{90} + X_0(\lambda, \phi) + \epsilon(\lambda, \phi, t)$$

359

360 where  $\lambda$  and  $\phi$  are the longitude and latitude,  $t$  is the time,  $\alpha$  and  $\beta$  are  
 361 the linear regression coefficients for 0° and 90° phases respectively,  $X_0$  and  $\epsilon$   
 362 are the constant and error terms respectively.

363 We evaluated statistical significance using a two-sided t-test and, in the  
 364 case of regression maps, p-values were adjusted by controlling for the False  
 365 Discovery Rate (Benjamini and Hochberg, 1995; Wilks, 2016) to avoid mis-  
 366 leading results from the high number of regressions (Walker, 1914; Katz and  
 367 Brown, 1991).

368

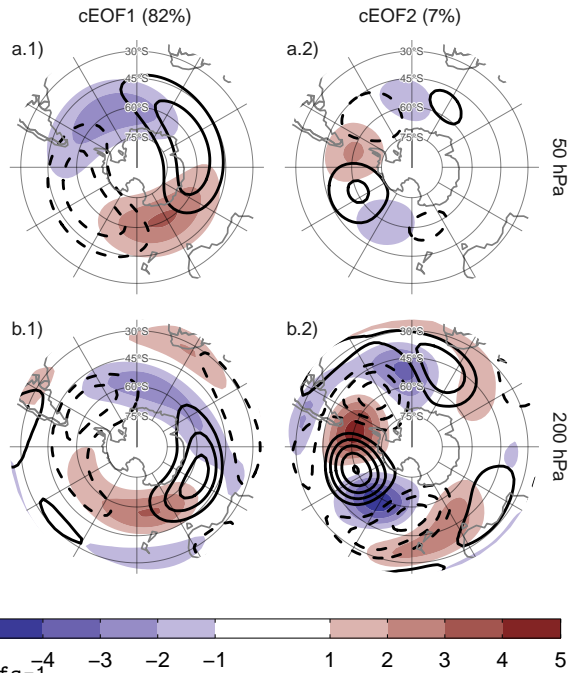


**Fig. 2:** Spatial patterns for the two leading cEOFs of SON geopotential height zonal anomalies at 50 hPa and 200 hPa for the 1979 – 2019 period. The shading (contours) corresponds to 0° (90°) phase. Arbitrary units. The proportion of variance explained for each mode with respect to the zonal mean is indicated in parenthesis.

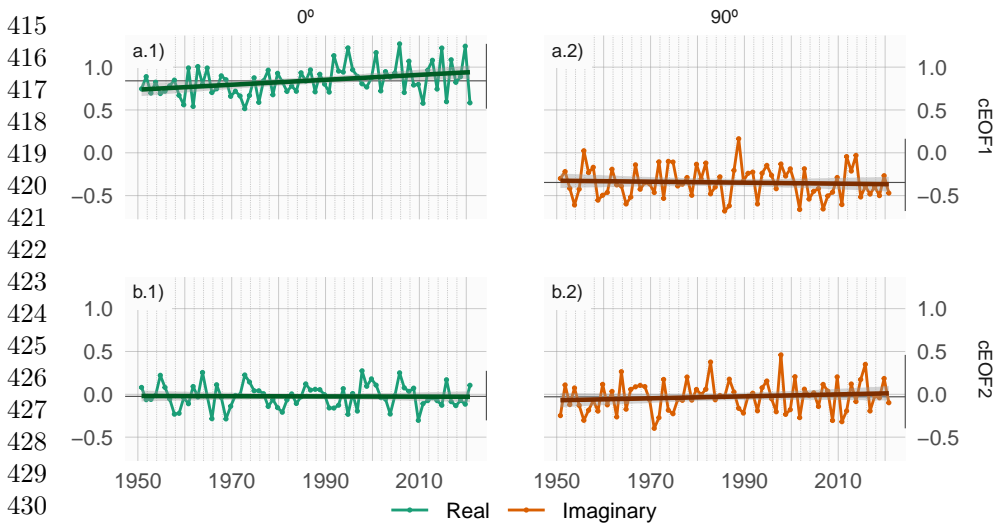
## 2.4 Computation procedures

We performed all analysis in this paper using the R programming language ([R Core Team, 2020](#)), using `data.table` ([Dowle and Srinivasan, 2020](#)) and `metR` ([Campitelli, 2020](#)) packages. All graphics are made using `ggplot2` ([Wickham, 2009](#)). We downloaded data from reanalysis using the `ecmwf.r` package ([Hufkens, 2020](#)) and indices of ENSO and Indian Ocean Dipole (IOD) with the `rsoi` package ([Albers and Campitelli, 2020](#)). The paper was rendered using `knitr` and `rmarkdown` ([Xie, 2015; Allaire et al, 2020](#)).

## 3 Results

### 3.1 cEOF spatial patterns

To describe the variability of the circulation zonal anomalies, the spatial and temporal parts of the first two leading cEOFs of zonal anomalies of geopotential height at 50 hPa and 200 hPa, computed jointly at both levels, are shown in Figures 2 and 3. The first mode (cEOF1) explains 82% of the variance of the zonally anomalous fields, while the second mode (cEOF2) explains a smaller

10 *SH zonally asymmetric circulation with cEOF*

**Fig. 3:** Time series of the two leading cEOFs of SON geopotential height zonal anomalies at 50 hPa and 200 hPa. cEOF1 (row a) and cEOF2 (row b) separated in their  $0^\circ$  (column 1) and  $90^\circ$  (column 2) phase. Dark straight line is the linear trend. Black horizontal and vertical line mark the mean value and range of each time series.

fig:extended-series

fraction (7%). In the spatial patterns (Fig. 2), the  $0^\circ$  and the  $90^\circ$  phases are in quadrature by construction, so that each cEOF describe a single wave-like pattern whose amplitude and position (i.e. phase) is controlled by the magnitude and phase of the temporal cEOF. The wave patterns described by these cEOFs match the patterns seen in the standard EOFs of Figure 1.

The cEOF1 (Fig. 2 column 1) is a hemispheric wave 1 pattern with maximum amplitude at high latitudes. At 50 hPa the  $0^\circ$  cEOF1 has the maximum of the wave 1 at  $150^\circ\text{E}$  and at 200 hPa, the maximum is located at around  $175^\circ\text{E}$  indicating a westward shift with height. The cEOF2 (Fig. 1 column 2) shows also a zonal wave-like structure with maximum amplitude at high latitudes, but with shorter spatial scales. In particular, the dominant structure at both levels is a wave 3 but with larger amplitude in the pacific sector. There is no apparent phase shift with height but the amplitude of the pattern is greatly reduced in the stratosphere, which is consistent with the fact that the cEOF2 computed separately for 200 hPa explains a bit more variance than the cEOF2 computed separately for 50 hPa (11% vs. 3%, respectively). This suggest that this barotropic mode represents mainly tropospheric variability.

There is no significant simultaneous correlation between cEOFs time series. Both cEOFs show year-to-year variability but show no evidence of decadal variability (Fig. 3). Because the geopotential fields that enter into the cEOFs algorithm are anomalies with respect to the zonal mean instead of the time mean, the cEOFs time series have non zero temporal mean. However, cEOF2

temporal mean is almost zero, which indicates that only cEOF1 includes variability that significantly projects onto the mean zonally anomalous field. This is consistent with the fact that the mean zonally anomalous field of geopotential height is very similar to the cEOF1 ( $r^2 = 98\%$ ) and not similar to the cEOF2 ( $r^2 = 0\%$ ). 461  
462  
463  
464  
465

A significant positive trend in the  $0^\circ$  phase of cEOF1 is evident (Fig. 3a.1, p-value = 0.0037) while there is no significant trend in any of the phases of cEOF2. The positive trend in the  $0^\circ$  cEOF1 translates into a positive trend in cEOF1 magnitude, but not systematic change in phase (not shown). This long-term change indicates an increase in the magnitude of the high latitude zonal wave 1.

### 3.2 cEOFs Regression maps

### 3.2.1 Geopotential

In the previous section, cEOF analysis was applied to zonal anomalies derived by removing the zonally mean values in order to isolate the main characteristics of the main zonal waves characterizing the circulation in the SH. In this section we compute regression fields using the full fields of the variables in order to describe the influence of the cEOFs on the temporal anomalies.

Figure 4 shows regression maps of SON geopotential height anomalies upon cEOF1. At 50 hPa (Figure 4 row a), the  $0^\circ$  cEOF1 is associated with a positive centre located over the Ross Sea. The  $90^\circ$  cEOF1 is associated with a distinctive wave 1 pattern with maximum over the coast of East Antarctica. At 200 hPa (Figure 4 row b) the  $0^\circ$  cEOF1 shows a single centre of positive anomalies spanning West Antarctica surrounded by opposite anomalies in lower latitudes, with its centre shifted slightly eastward compared with the upper-level anomalies. The  $90^\circ$  cEOF1 shows a much more zonally symmetrical pattern resembling the negative SAM phase (e.g. Fogt and Marshall, 2020). Therefore, the magnitude and phase of the cEOF1 are associated with the magnitude and phase of a zonal wave mainly in the stratosphere.

Figure 5 shows the regression maps of geopotential height anomalies upon the cEOF2. In the troposphere (Fig. 5 row a) the regression maps show wave trains similar to those identified for cEOF2 patterns (Fig 2). Regressed anomalies associated with the  $0^\circ$  cEOF2 are  $1/4$  wavelength out of phase with those associated with the  $90^\circ$  cEOF2. All fields have a dominant zonal wave 3 limited to the western hemisphere, over the Pacific and Atlantic Oceans. cEOF2 then represents an equivalent barotropic wave train that is very similar to the the PSA Patterns ([Mo and Paegle, 2001](#)). Comparing the location of the positive anomaly near  $90^\circ\text{W}$  in column 2 of Figure 5 with Figures 1.a and b from [Mo and Paegle \(2001\)](#), the  $0^\circ$  cEOF2 regression map could be identified with PSA2, while the  $90^\circ$  cEOF2 resembles PSA1.

These wave patterns are also present in the stratosphere (Fig. 5 row a) supporting their equivalent barotropic nature. But also present is a monopole over the pole with negative sign associated with the  $0^\circ$  cEOF2 and positive sign

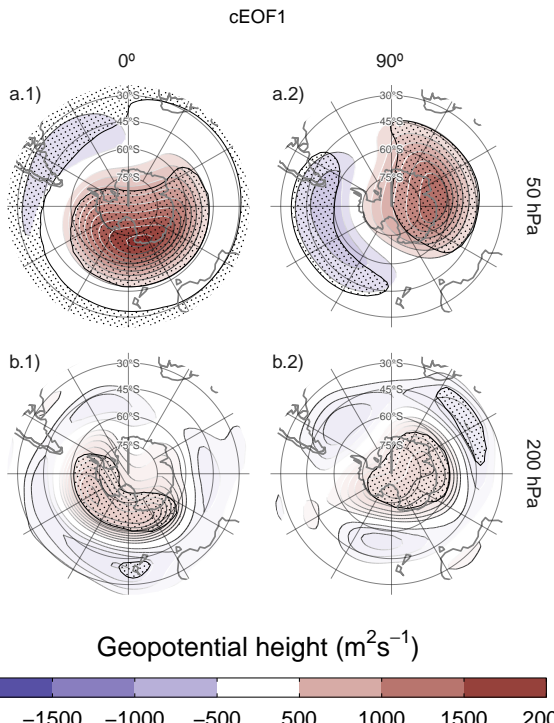


**Fig. 4:** Regression of SON geopotential height anomalies ( $m^2 s^{-1}$ ) with the (column 1)  $0^\circ$  and (column 2)  $90^\circ$  phases of the first cEOF for the 1979 – 2019 period at (row a) 50 hPa and (row b) 200 hPa. These coefficients come from multiple linear regression involving the  $0^\circ$  and  $90^\circ$  phases. Areas marked with dots have p-values smaller than 0.01 adjusted for False Detection Rate.

associated with the  $90^\circ$  cEOF2. This monopole might indicate strengthening of the polar vortex associated with positive values of the  $0^\circ$  cEOF2 and weakening associated with negative values of  $0^\circ$  cEOF2. However, since these anomalies are not statistically significant, this feature should not be overinterpreted.

### 3.2.2 Temperature and Ozone

The signature of cEOFs variability on air temperature was also evaluated. Figure 6 shows regression maps of air temperature anomalies at 50 hPa and 200 hPa upon cEOF1. The distribution of temperature regression coefficients at 50 hPa and at 200 hPa mirror the geopotential height regression maps at 50 hPa (Fig. 4). In both levels, the  $0^\circ$  cEOF1 is associated with a positive centre over the South Pole with its centre moved slightly towards  $150^\circ\text{E}$  (Fig. 6 column 1). On the other hand, the regression maps on the  $90^\circ$  cEOF1 show a clearer wave 1 pattern with its maximum around  $60^\circ\text{E}$ .

Figure 7 shows the vertical distribution of the regression coefficients on cEOF1 from zonal anomalies of air temperature and of ozone mixing ratio

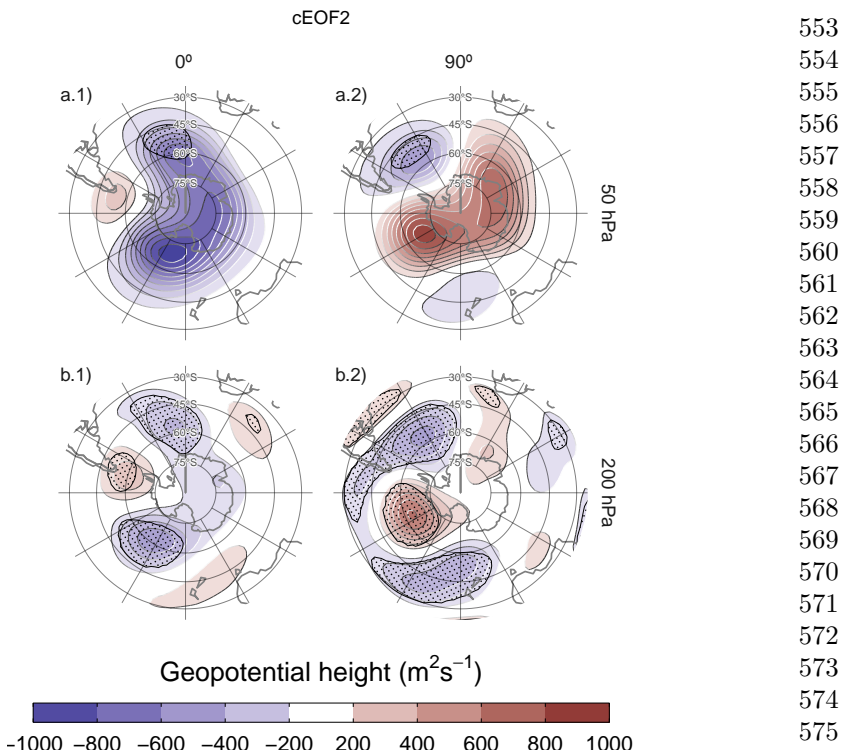


**Fig. 5:** Same as Figure 4 but for cEOF2.

averaged between 75°S and 45°S. Temperature zonal anomalies associated with cEOF1 show a clear wave 1 pattern for both 0° and 90° phases throughout the atmosphere above 250 hPa with a sign reversal above 10 hPa. As a result of the hydrostatic balance, this is the level in which the geopotential anomaly have maximum amplitude (not shown).

The maximum ozone regressed anomalies coincide with the minimum temperature anomalies above 10 hPa and with the maximum temperature anomalies below 10 hPa (Fig. 7). Therefore, the ozone zonal wave 1 is negatively correlated with the temperature zonal wave 1 in the upper stratosphere, and positively correlated in the upper stratosphere. This change in phase is observed in ozone anomalies forced by planetary waves that reach the stratosphere. In the photochemically-dominated upper stratosphere, cold temperatures inhibit the destruction of ozone, explaining the opposite behaviour for both variables as were elucidated with dynamical chemical models (Hartmann and Garcia, 1979; Wirth, 1993; Smith, 1995). On the other hand, in the advectively-dominated lower stratosphere, ozone anomalies are 1/4 wavelength out of phase with horizontal and vertical transport, which are in addition 1/4 wavelength out of phase with temperature anomalies, resulting in same sign

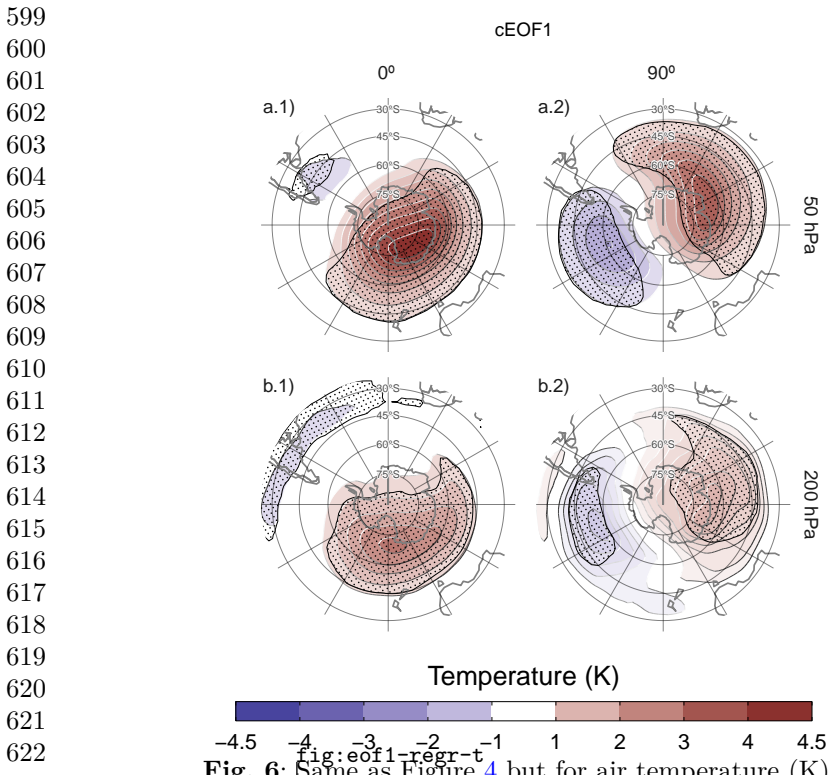


**Fig. 6:** Same as Figure 4 but for air temperature (K).

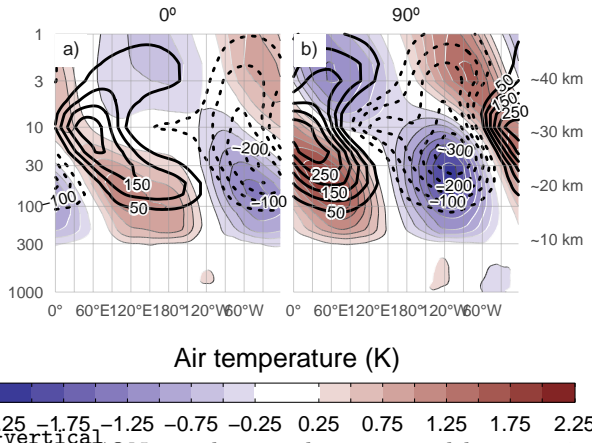


**Fig. 7:** Regression of SON zonal anomalies averaged between 75°S and 45°S of mean air temperature (shaded, Kelvin) and ozone mixing ratio (contours, negative contours with dashed lines, labels in parts per billion by mass) with the (a) 0° and (b) 90° phase of the cEOF1 for the 1979 – 2019 period.

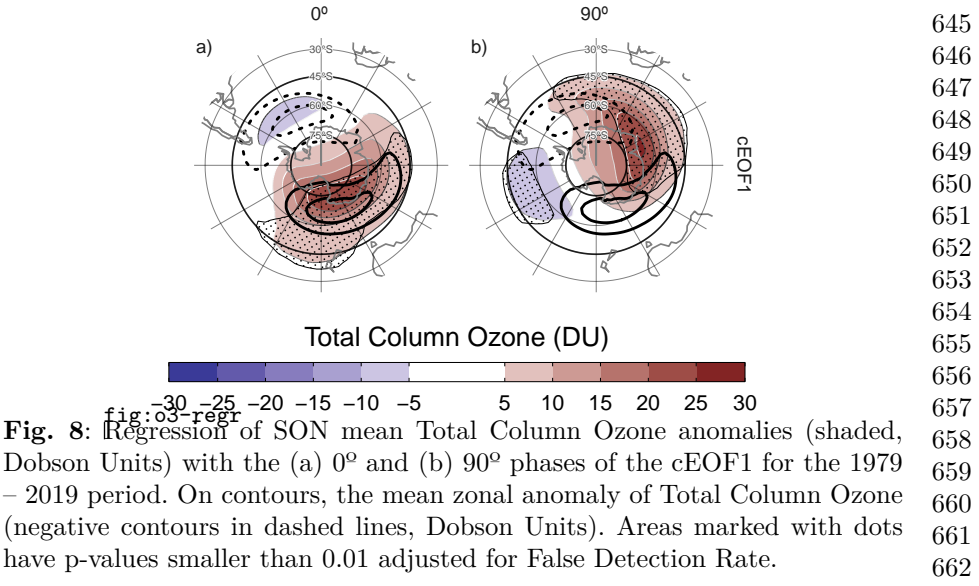


**Table 2:** Correlation coefficients ( $r$ ) between cEOF2 components and the PSA1 and PSA2 modes computed as [Mo and Paegle \(2001\)](#) for the 1979 – 2019 period. 95% confidence intervals in parenthesis. p-values lower than 0.01 in bold.

PC	cEOF2	
	Real	Imaginary
PSA1	0.26 (CI: -0.04 – 0.52)	<b>0.82 (CI: 0.69 – 0.9)</b>
PSA2	<b>0.79 (CI: 0.63 – 0.88)</b>	-0.02 (CI: -0.32 – 0.29)

anomalies for the response of both variables ([Hartmann and Garcia, 1979](#); [Wirth, 1993](#); [Smith, 1995](#)).

The regression maps of TOC anomalies upon cEOF1 (Fig. 8) show zonal wave 1 patterns associated with both components of cEOF1. The climatological position of the springtime Ozone minimum (ozone hole) is outside the South Pole and towards the Weddell Sea (e.g. [Grytsai, 2011](#)). Thus, the 0° cEOF1 regression field (Figure 8a) coincides with the climatological position of the ozone hole, while it is 90° out of phase for the 90° cEOF1. The temporal correlation between the amplitudes of TOC planetary wave 1 and the amplitude of cEOF1 is 0.79 (CI: 0.63 – 0.88), while the correlation between their phases is -0.85 (CI: -0.92 – -0.74). Consequently, cEOF1 is strongly related with the SH ozone variability.

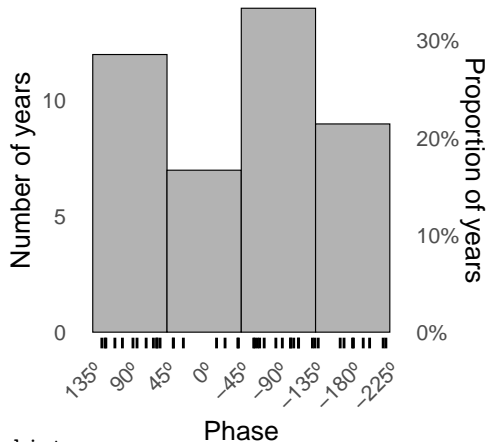


**Fig. 9:** `fig:phase-histogram` Histogram of phase distribution of cEOF2 phase for the 1979 – 2019 period. Bins are centred at  $90^\circ$ ,  $0^\circ$ ,  $-90^\circ$ ,  $-180^\circ$  with a binwidth of  $90^\circ$ . The small vertical lines near the horizontal axis mark the observations.

### 3.3 PSA

Given the similarity between the cEOF2 related-associated structures (Fig. 5) and documented PSA patterns, we study the relationship between them. Table 2 shows the correlations between the two PSA indices and the time series for  $0^\circ$  and  $90^\circ$  phases of cEOF2. As visually anticipated by Figure 5, there is a large positive correlation between PSA1 and  $90^\circ$  cEOF2, and between PSA2 and  $0^\circ$  cEOF2. On the other hand, there is no significant relationship between PSA1 and  $0^\circ$  cEOF2, and between PSA2 and  $90^\circ$  cEOF2. As a result, cEOF2 represents well both the spatial structure and temporal evolution of the PSA modes, so it is possible to make an association between its two phases and the two PSA modes. That is, the phase election for cEOF2 that maximises the relationship between ENSO and  $90^\circ$  cEOF2, also maximises the association between cEOF2 components and PSA modes (not shown).

Figure 9 shows an histogram that counts the number of SON seasons in which the cEOF2 phase was close to each of the four particular phases (positive/negative of  $0^\circ$  and  $90^\circ$  phases), with the observations for each season marked as rugs on the horizontal axis. In 62% of seasons cEOF2 has a phase similar to either the negative or positive  $90^\circ$  phase, making the  $90^\circ$  phase the most common phase. This is also the phase that is most correlated with ENSO by the definition of the  $0^\circ$  phase as described in Section 2.

Therefore, by virtue of being the most common phase, the  $90^\circ$  cEOF2 explains more variance than the  $0^\circ$  cEOF2. Conventional EOF analysis will therefore tend to separate them relatively cleanly, with the EOF representing the  $90^\circ$  cEOF2 always leading the one representing the  $0^\circ$  cEOF2. This phase preference is in agreement with Irving and Simmonds (2016), who found a

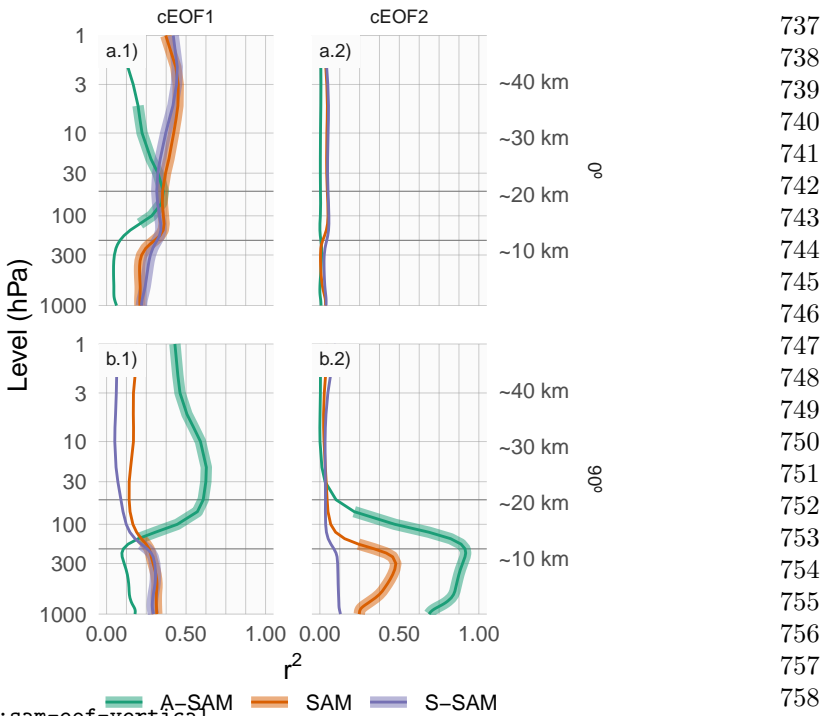


**Fig. 10:** Coefficient of determination ( $r^2$ ) between each component of cEOFs and the SAM, Asymmetric SAM (A-SAM) and Symmetric SAM (S-SAM) indices computed at each level for the 1979 – 2019 period. Thick lines represent estimates with  $p$ -value  $< 0.01$  corrected for False Detection Rate (Benjamini and Hochberg, 1995).

bimodal distribution to PSA-like variability (compare our Figure 9 with their Figure 6).

### 3.4 SAM

We now explore the relationship between SAM and the cEOFs motivated by the resemblance between cEOFs regression maps and SAM patterns shown in Section 3.2. We computed the coefficient of determination between the cEOFs time series and the three SAM indices (SAM, A-SAM and S-SAM) defined by Campitelli et al (2022b) at each vertical level (Fig. 10). The SAM index is statistically significantly correlated with the  $0^\circ$  cEOF1 in all levels, and with the  $90^\circ$  cEOF1 and  $90^\circ$  cEOF2 in the troposphere. On the other hand, correlations between SAM and the  $0^\circ$  cEOF2 are non-significant.

The relationship between the SAM and cEOF1 in the troposphere is explained entirely by the zonally symmetric component of the SAM as shown by the high correlation with the S-SAM below 100 hPa and the low and statistically non-significant correlations between the A-SAM and either the  $0^\circ$

18 *SH zonally asymmetric circulation with cEOF*

783 or 90° cEOF1. In the stratosphere, the 0° cEOF1 is correlated with both A-  
 784 SAM and S-SAM, while the 90° cEOF1 is highly correlated only with the  
 785 A-SAM. These correlations are consistent with the regression maps of geopo-  
 786 tential height in Figure 4 and their comparison with those obtained for SAM,  
 787 A-SAM and S-SAM by [Campitelli et al \(2022b\)](#).

788 In the case of 90° cEOF2, its correlation with the SAM for the troposphere  
 789 is associated to the asymmetric variability of the SAM. Indeed, the 90° cEOF2  
 790 shares up to 92% variance with the A-SAM and only 12% at most with the  
 791 S-SAM (Figure 10.b2). Such extremely high correlation between A-SAM and  
 792 90° cEOF2 suggests that the modes obtained in this work are able to charac-  
 793 terise the zonally asymmetric component of the SAM described previously by  
 794 [Campitelli et al \(2022b\)](#).

795

796 

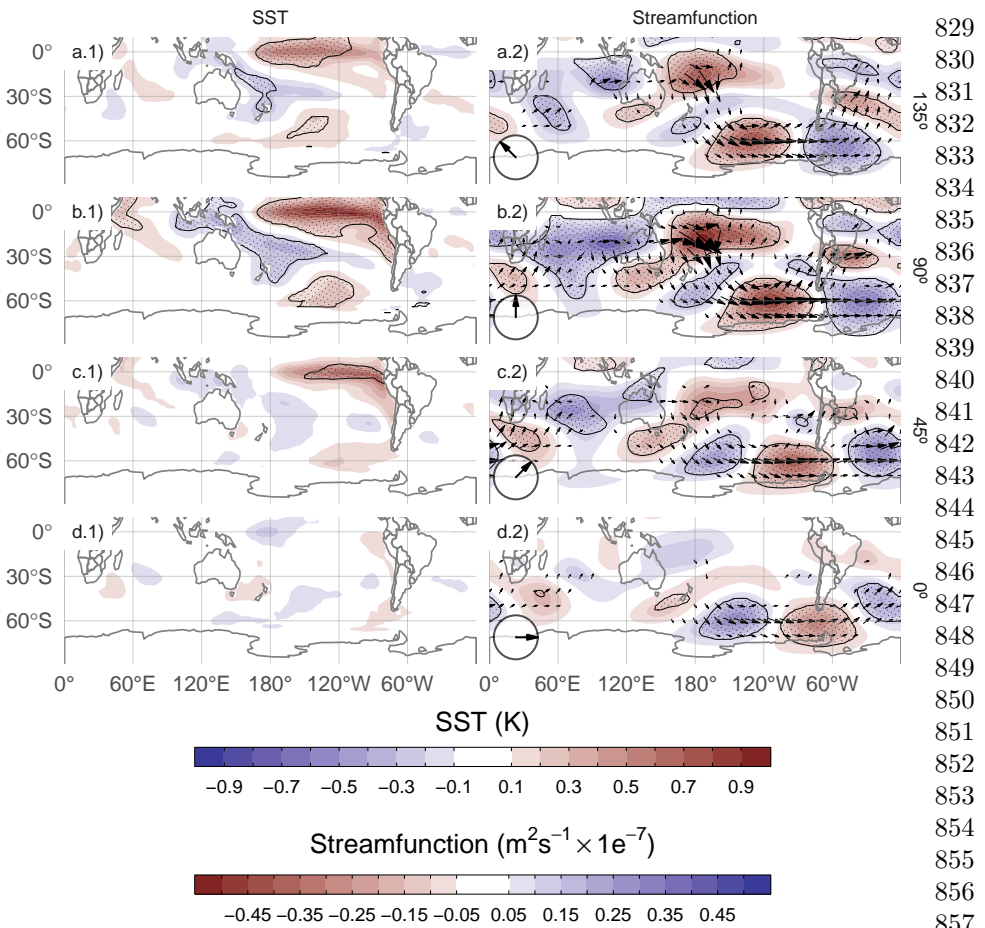
### 3.5 Tropical sources of cEOFs variabitliy

797 The connections between cEOFs and tropical sources of variability were also  
 798 assessed. Figure 11 shows the regression maps of Sea Surface Temperature  
 799 (SST) and streamfunction anomalies at 200 hPa upon standardised cEOF2.  
 800 As well as regression maps for the 0° and 90° phases, we include corresponding  
 801 regressions for two intermediate directions (corresponding to 45° and 135°).

802 The 90° cEOF2 (second row) is associated with strong positive SST anom-  
 803 alies on the Central to Eastern Pacific and negative anomalies over an area  
 804 across northern Australia, New Zealand the South Pacific Convergence Zone  
 805 (SPCZ) (Figure 11.b1). The regression field of SST anomalies bears a strong  
 806 resemblance with canonically positive ENSO ([Bamston et al, 1997](#)). Indeed,  
 807 there is a significant and very high correlation (0.76 (CI: 0.6 – 0.87)) between  
 808 the ONI and the 90° cEOF2 time series. In addition to the Pacific ENSO-like  
 809 pattern, there are also positive anomalies in the western Indian Ocean and  
 810 negative values in the eastern Indian Ocean, resembling a positive IOD ([Saji  
 811 et al, 1999](#)). Consistently, the correlation between the 90° cEOF2 and the DMI  
 812 is 0.62 (CI: 0.38 – 0.78).

813 The 90° cEOF2 is associated with strong wave-like streamfunction anom-  
 814 alies emanating from the tropics (Figure 11.b2), both from the Central Pacific  
 815 sector and the Indian Ocean. The atmospheric response associated with 90°  
 816 cEOF2 is then consistent with the combined effect of ENSO and the IOD on  
 817 the extratropics: with SST anomalies inducing anomalous tropical convection  
 818 that in turn excite Rossby waves propagating meridionally towards higher  
 819 latitudes ([Mo, 2000; Cai et al, 2011a; Nuncio and Yuan, 2015](#)).

820 However, the cEOF2 is not associated with the same tropical SST anomaly  
 821 patterns at all their phases Figure 11.d1 and d2 show that the 0° cEOF2 is  
 822 not associated either with any significant SST nor streamfunction anomalies  
 823 in the tropics. As a result, the correlation between the 0° cEOF2 and ENSO  
 824 is not significant (0 (CI: -0.3 – 0.3)). Meanwhile, Rows a and c in Fig. 11 show  
 825 that the intermediate phases are still associated with significant SST regressed  
 826 anomalies over the Pacific Ocean, but at slightly different locations. The 135°  
 827 phase is associated with SST anomalies in the central Pacific (Fig. 11a.1),  
 828



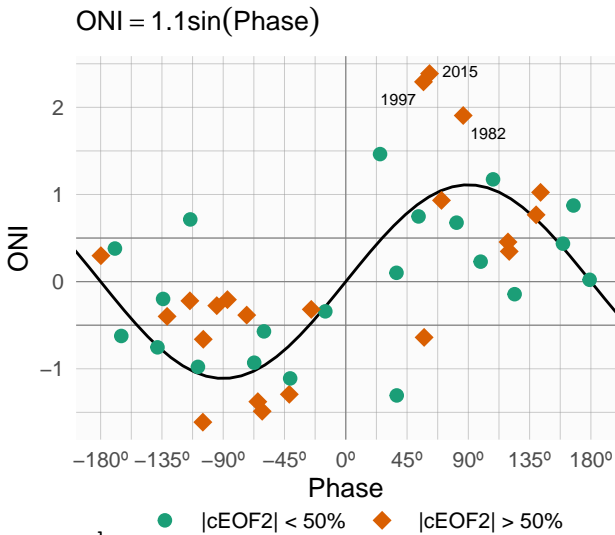
**Fig. 11:** Regression of SST (K, left column) and streamfunction zonal anomalies ( $m^2/s \times 10^{-7}$ , shaded) with their corresponding activity wave flux (vectors) (right column) upon cEOF2 different phases (illustrated in the lower-left arrow) for the 1979 – 2019 period. Areas marked with dots have p-values smaller than 0.01 adjusted for FDR.

fig:sst-psi-2

while the  $45^\circ$  phase is associated with SST anomalies that correspond roughly to the Central Pacific and Eastern Pacific “flavours” of ENSO, respectively (Fig. 11c.1) (Kao and Yu, 2009). Both phases are also associated to wave trains generated in the region surrounding Australia and propagates toward the extra-tropics, although less intense than the ones associated with the  $90^\circ$  phase.

To further explore the relationship between tropical forcing and phases of the cEOF2, Figure 12 shows the ONI plotted against the cEOF2 phase for each SON trimester between 1979 and 2019, highlighting years in which the magnitude of cEOF2 is above the median. In years with positive (negative)

829  
830  
831  
832  
833  
834  
835  
836  
837  
838  
839  
840  
841  
842  
843  
844  
845  
846  
847  
848  
849  
850  
851  
852  
853  
854  
855  
856  
857  
858  
859  
860  
861  
862  
863  
864  
865  
866  
867  
868  
869  
870  
871  
872  
873  
874



**Fig. 12:** fig:enso-phase SON ONI values plotted against cEOF2 phase for the 1979 – 2019 period. Years with magnitude of cEOF2 greater (smaller) than the 50th percentile are shown as orange diamonds (green circles). Black line is the fit  $\text{ONI} \sim \sin(\text{phase})$  computed by weighted OLS using the magnitude of the cEOF2 as weights.

ONI, the cEOF2 phase is mostly around  $90^\circ$  ( $-90^\circ$ ). In the neutral ENSO seasons, the cEOF2 phase is much more variable. The black line in Figure 12 is a sinusoidal fit of the relationship between ONI and cEOF2 phase. The  $r^2$  corresponding to the fit is 0.57, statistically significant with p-value  $< 0.001$ , indicating a quasi-sinusoidal relation between these two variables.

The correlation between the absolute magnitude of the ONI and the cEOF2 amplitude is 0.45 (CI: 0.17 – 0.66). However, this relationship is mostly driven by the three years with strongest ENSO events in the period (2015, 1997, and 1982) which coincide with the three years with strongest cEOF2 magnitude (not shown). If those years are removed, the correlation becomes non-significant (0.04 (CI: -0.28 – 0.35)). Furthermore, even when using all years, the Spearman correlation –which is robust to outliers– is also non-significant (0.2, p-value = 0.21). Therefore, although the location of tropical SST anomalies seem to have an effect in defining the phase of the cEOF2, the relationship between the magnitude of cEOF2 and ONI remains uncertain and might be only evident in very strong ENSO events, that are scarce in the historical observational record.

We conclude that the wave train represented by cEOF2 can be both part of the internal variability of the extratropical atmosphere and forced by tropical SSTs. In the former case, the wave train has little phase preference. However, when cEOF2 is excited by tropical SST variability, it tends to remain locked to

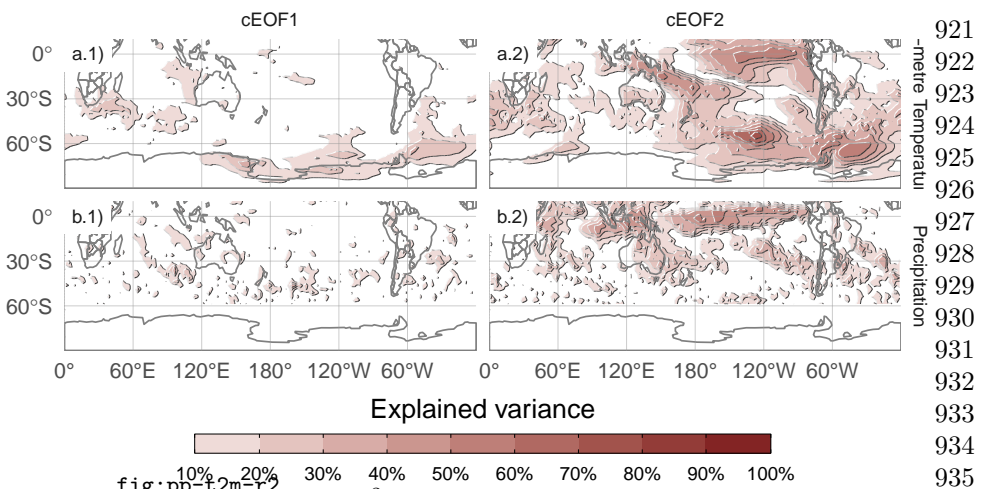


**Fig. 13:** Explained variance ( $r^2$  as percentage) of 2-metre temperature (row a) and precipitation (row b) anomalies by the regression upon cEOF1 (column 1) and cEOF2 (column 2).

the  $90^\circ$  phase. This explains the relative over-abundance of years with cEOF2 near positive and negative  $90^\circ$  phase in Figure 9.

Unlike the cEOF2 case, there are no significant SST regressed anomalies associated with either the  $0^\circ$  or  $90^\circ$  cEOF1 (Sup. Figure A.1). Consistently, streamfunction anomalies do not show any tropical influence. Instead, the  $0^\circ$  and  $90^\circ$  cEOF1 are associated with zonally propagating wave activity fluxes in the extra-tropics around  $60^\circ\text{S}$ , except for an equatorward flow from the coast of Antarctica around  $150^\circ\text{E}$  in the  $0^\circ$  phase. This suggests that the variability of cEOF1 is driven primary by the internal variability of the extra-tropics.

### 3.6 cEOFs surface impacts

The influence of cEOFs variability in the anomalies of both 2-metre air temperature and precipitation in the SH was also explored. Figure 13 shows the 2-meter temperature and precipitation anomalies explained variance by the multiple linear model of both  $0^\circ$  and  $90^\circ$  cEOF1 (column 1), and both  $0^\circ$  and  $90^\circ$  cEOF2 (column 2). The variance explained by cEOF1 for precipitation anomalies and temperature anomalies in most regions is extremely low, except for the northern tip of the Antarctic Peninsula, northern Weddell Sea and the Ross Sea coast (Fig. 13a.1).

This lack of strong relationship between the cEOF1 and SST, temperature and precipitation might be surprising considering the correlation between the cEOF1 and the SAM (Fig. 10 column 1) and the correlation between SAM and Central Pacific SST, temperature east and west of the Antarctic Peninsula, and with precipitation in western Australia (Fogt and Marshall, 2020). There are two main reasons for this. First, the correlation between cEOF1

precipitation

921  
922  
923  
924  
925  
926  
927  
928  
929  
930  
931  
932  
933  
934  
935  
936  
937  
938  
939  
940  
941  
942  
943  
944  
945  
946  
947  
948  
949  
950  
951  
952  
953  
954  
955  
956  
957  
958  
959  
960  
961  
962  
963  
964  
965  
966

22 *SH zonally asymmetric circulation with cEOF*

967 and the SAM in the troposphere is modest, with less than 50% of shared variance  
 968 (Fig. 10 column 1), so these indices are not expected to be equivalent.  
 969 Second, Campitelli et al (2022b) showed that the strong relationship between  
 970 the SAM and Pacific SSTs and temperature anomalies around the Antarctic  
 971 Peninsula is mainly due to the asymmetric part of the SAM. Meanwhile, the  
 972 cEOF1 is significantly correlated only with the symmetric part of the SAM  
 973 (Fig. 10 column 1), which by itself is not significantly correlated with surface  
 974 temperatures in that area.

975 On the other hand, the cEOF2 explained variance is greater than 50% in  
 976 some regions for both variables (Fig. 13 column 2). For 2-metre temperature,  
 977 there are high values in the tropical Pacific and the SPCZ, as well as the  
 978 region following an arc between New Zealand and the South Atlantic, with  
 979 higher values in the Southern Ocean. Over the continents, there are moderate  
 980 values of about 30% variance explained in southern Australia, Southern South  
 981 America and the Antarctic Peninsula. For precipitation, there are high values  
 982 over the tropics. At higher latitudes, moderate values are observed over eastern  
 983 Australia and some regions of southern South America.

984 Since the cEOF1 has a relatively weak signal in the surface variables  
 985 explored here, we will only focus on the cEOF2 influence. Figure 14 shows  
 986 regression maps of 2-metre temperature (column 1) and precipitation (column  
 987 2) anomalies upon different phases of standardised cEOF2.

988 Temperature anomalies associated with the 90° cEOF (Fig. 14.b1) show  
 989 positive values in the tropical Pacific, consistent with SSTs anomalies associ-  
 990 ated with the same phase (Fig. 11.b1). At higher latitudes there is a wave-like  
 991 pattern of positive and negative values that coincide with the nodes of the  
 992 850 hPa geopotential height regression patterns. This is consistent with tem-  
 993 perature anomalies produced by meridional advection of temperature by the  
 994 meridional winds arising from geostrophic balance. Over the continents, the  
 995 90° cEOF2 (Fig. 14b.1) is associated with positive regressed temperature  
 996 anomalies in southern Australia and negative regressed anomalies in south-  
 997 ern South America and the Antarctic Peninsula, that are a result of the wave  
 998 train described before.

999 The temperatures anomalies associated with the 0° cEOF2 (Fig. 14d.1)  
 1000 are less extensive and restricted to mid and high latitudes.

1001 Over the continents, the temperature anomalies regressions are non significant,  
 1002 except for positive anomalies near the Antarctic Peninsula.

1003 Tropical precipitation anomalies associated with the 90° cEOF2 are strong,  
 1004 with positive anomalies in the central Pacific and western Indian, and negative  
 1005 anomalies in the eastern Pacific (Fig. 14b.2). This field is consistent with  
 1006 the SST regression map (Fig. 14b.1) as the positive SST anomalies enhance  
 1007 tropical convection and the negative SST anomalies inhibits it.

1008 In the extra-tropics, the positive 90° cEOF2 is related to drier conditions  
 1009 over eastern Australia and the surrounding ocean, that it is similar signal as  
 1010 the one associated with ENSO (Cai et al, 2011a). However, the 90° cEOF2  
 1011 is not the phase most correlated with precipitation in that area. The 135°  
 1012

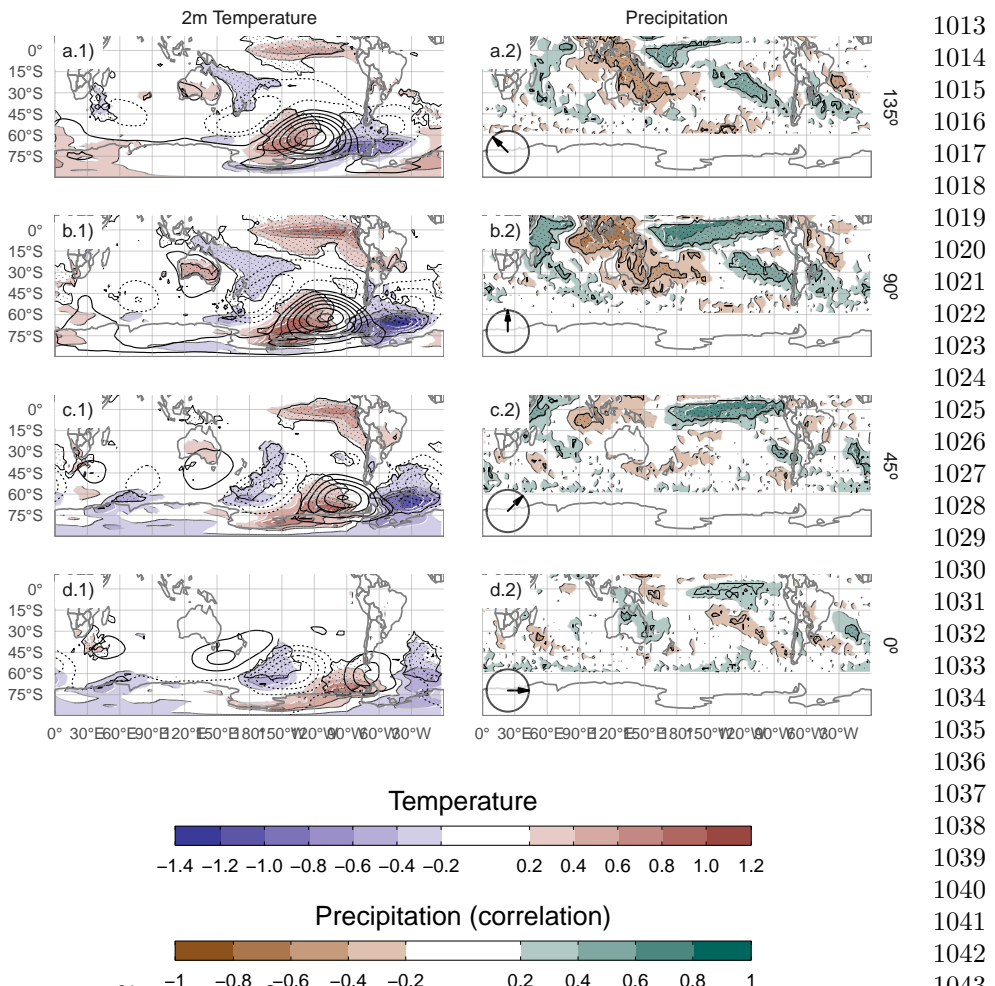


**Fig. 14:** `fig:pp-temp-2`: Regression of SON mean 2-meter temperature (K, shaded) and 850 hPa geopotential height (m, contours) (column 1), and precipitation (correlation, column 2) upon different phases of cEOF2. For the 1979 – 2019. Areas marked with dots have p-values smaller than 0.01 adjusted for False Detection Rate.

phase (an intermediate between positive  $90^\circ$  and  $180^\circ$  cEOF2) component is associated with stronger and more extensive temporal correlations with precipitation over Australia and New Zealand. The influence of cEOF2 in Australian precipitation could be more related to the direct impacts of SST anomalies in the surrounded oceans rather than on the interconnection pattern represented by the cEOF2.

Over South America, the  $90^\circ$  cEOF2 has positive correlations with precipitation in South Eastern South America (SESA) and central Chile, and negative

1059 correlations in eastern Brazil. This correlation field matches the springtime  
 1060 precipitation signature of ENSO (e.g. Cai et al., 2020) and it is also similar  
 1061 to the precipitation anomalies associated with the A-SAM (Campitelli et al.,  
 1062 2022b). This result is not surprising considering the close relationship of the  
 1063 90° cEOF2 with both ONI and A-SAM index, which was shown previously.  
 1064 Furthermore, it consolidates the identification of the cEOF2 with the PSA  
 1065 pattern. Resembling the relationship between ONI and the phase of cEOF2  
 1066 (Fig. 12), there is a cEOF2 phase dependence of the precipitation anomalies  
 1067 in SESA (not shown).

1068 The correlation coefficients between precipitation anomalies and the 0°  
 1069 cEOF2 (Fig. 14d.2) are weaker than for 90° cEOF2. There is a residual pos-  
 1070 itive correlation in the equatorial eastern Pacific and small, not statistically  
 1071 significant positive correlations over eastern Australia and negative ones over  
 1072 New Zealand.

1073

## 1074 4 Discussion and conclusions

1075

discussion

1076 In this study we assessed extratropical Southern Hemisphere zonally asym-  
 1077 metric circulation in austral spring. For this purpose, we derived two complex  
 1078 indices using Complex Empirical Orthogonal Functions and used to charac-  
 1079 terise both amplitude and phase of planetary waves.

1080 The cEOF1 represents the variability of the zonal wave 1 in the strato-  
 1081 sphere and is closely related to stratospheric variability such as anomalies in  
 1082 Total Column Ozone. Otherwise, this complex EOF is not related with SST  
 1083 variability and continental precipitation in the Southern Hemisphere. On the  
 1084 other hand, the cEOF2 represents a wave-3 pattern with maximum magnitude  
 1085 in the Pacific sector, that is an alternative representation of the PSA1 and  
 1086 PSA2 patterns (Mo and Paegle 2001). The 90° cEOF2 can be identified with  
 1087 the PSA1 and the 0° cEOF2 with the PSA2. While the cEOF2 variability is  
 1088 related to surface impacts, the cEOF1 surface influence is almost negligible.  
 1089 For instance, precipitation anomalies in South America associated with the  
 1090 90° cEOF2 show a clear ENSO-like impact, with positive anomalies in South-  
 1091 eastern South America, negative anomalies in Southern Brazil and positive  
 1092 anomalies in central Chile for positive 90° cEOF2 phase.

1093 Variability patterns that arise from cEOF methodology describe the zon-  
 1094 ally asymmetric springtime extratropical SH circulation, reproducing previous  
 1095 features such as the variability related to PSAs or A-SAM.

1096 Since the spatial fields obtained from both components of cEOF2, which  
 1097 resemble PSA patterns, are in quadrature by construction, the cEOF method-  
 1098 ology allows to derive, for the first time to our knowledge, a joint PSA  
 1099 index from the resulted amplitude and phase. These patterns are not forced  
 1100 to be orthogonal to other modes of circulation, like they are in standard  
 1101 EOF methodology. This allows us to show for example, that the 90° cEOF2,  
 1102 corresponding to PSA1 variability, is closely associated to the SAM in the  
 1103 troposphere. Previous research in the SAM-PSA relationship had the issue  
 1104

that the SAM and the PSA patterns are not independently derived and so the correlation between these indices had to be zero by construction. 1105  
 Most studies on the relationship between ENSO and SAM rely on correlations 1106  
 between an ENSO index and the SAM index (e.g. L'Heureux and 1107  
 Thompson, 2006, Cai et al (2011b)) or between the SAM index and other 1108  
 variables associated with tropical convection, such as OLR or tropical SSTS 1109  
 (e.g. Carvalho et al, 2005). However, Campitelli et al (2022b) showed that the 1110  
 correlation between ENSO and SAM is almost completely explained by the 1111  
 asymmetric component of the SAM. In this work we show that the asymmetric 1112  
 component of the SAM can be identified with the PSA1. Therefore, the 1113  
 correlation between ENSO and SAM is predominantly the correlation between 1114  
 ENSO and PSA1. This sheds new light into the previous literature, as it cannot 1115  
 be assumed that a high correlation between ENSO and SAM indexes indicates 1116  
 a relationship between ENSO and zonally symmetric variability. 1117  
 1118

Further investigation is necessary to determine the connection between 1119  
 the symmetric component of the SAM and the PSA. It is possible that the 1120  
 PSA may force a zonally symmetric response (or vice versa) via wave-zonal 1121  
 mean flow interactions, or that this correlation is simply a statistical artefact 1122  
 resulting from the EOF methodology used to define the SAM and the fact 1123  
 that the spatial structure of the PSA projects onto the spatial structure of the 1124  
 symmetric SAM. 1125

Irving and Simmonds (2016) argued that there is some disagreement in the 1126  
 literature of whether the phase of the PSA pattern is affected by the location 1127  
 of tropical SST anomalies. With the methodology used in this study, we were 1128  
 able to show not only that the cEOF2 tends to be in the positive or negative 1129  
 90° phase (~PSA1) when the ENSO region is warm or cold, respectively, but 1130  
 also that central Pacific SST anomalies tend to align the cEOF towards the 1131  
 negative 0° phase and eastern Pacific SST anomalies tend to align it towards 1132  
 positive 0° phase. When ENSO phase is neutral, the cEOF2 is still as active, 1133  
 but with no preferred phase. The latter agrees with the results of Cai and 1134  
 Watterson (2002), who showed that the CSIRO Model can develop PSA-like 1135  
 variability even in the absence of ENSO forcing (i.e. with a climatological 1136  
 run), but that the variability of one of the PSA modes was enhanced when 1137  
 adding the ENSO signal. The sensitivity of the phase of the PSAs to the 1138  
 location of the tropical SST anomalies was also seen by Ciasto et al (2015), 1139  
 who detected similar Rossby wave patterns associated with central Pacific and 1140  
 eastern Pacific SST anomalies but with a change in phase. 1141

The method used in this study has similarities to the one used by Goyal 1142  
 et al (2022) as they construct an index of amplitude and phase of zonal 1143  
 wave 3-like variability by combining the two leading EOFs of meridional wind 1144  
 anomalies. The patterns obtained by them bear high resemblance with cEOF2. 1145  
 Although a detailed comparison is out of scope for this paper, the cEOF analysis 1146  
 has the advantage of constructing the indices based on patterns that are 1147  
 exactly in quadrature by construction. 1148

1149  
 1150

1151 The methodology proposed in this study allows for a deeper understanding  
 1152 of the zonally asymmetric springtime extratropical SH circulation such as a  
 1153 better description of PSA like variability using a unique complex index and the  
 1154 understanding of relationship between PSAs and ENSO or SAM variability.  
 1155 Further work should extend this analysis to other seasons and further study  
 1156 the relationship between the cEOF2 and the SAM.

1157

## 1158 **Declarations**

1159

declarations

### 1160 **Funding**

1161

funding

1162 The research was supported by UBACyT20020170100428BA, Consejo  
 1163 Nacional de Investigaciones Científicas y Técnicas (CONICET) PIP  
 1164 11220200102038CO, PICT-2020-SERIEA-I-INVI-00540, and the CLIMAX  
 1165 Project funded by Belmont Forum/ANR-15-JCL/-0002-01. Elio Campitelli  
 1166 was supported by a PhD grant from CONICET, Argentina.

1167

### 1168 **Conflict of interest/Competing interests**

1169

conflict-of-interestcompeting-interests

1170 The authors have no relevant financial or non-financial interests to disclose.

1170

### 1171 **Ethics approval**

1172

ethics-approval

1173 Not applicable.

1174

### 1175 **Consent to participate**

1176

consent-to-participate

1177 Not applicable.

1178

### 1179 **Consent for publication**

1180

consent-for-publication

1181 Not applicable.

1182

### **Availability of data and materials**

1183

availability-of-data-and-materials

1184 All data used in this paper available in a Zenodo repository ([Campitelli et al,](#)  
 1185 [2022a](#)) (<https://zenodo.org/record/6612429>). Indices updated monthly and  
 1186 daily will be made available at [http://www.cima.fcen.uba.ar/~elio.campitelli/  
 1187 shceof/](http://www.cima.fcen.uba.ar/~elio.campitelli/shceof/).

1188

It is also freely available from their respective sources:

1189

- ERA5 data can be obtained via the Copernicus Climate Data Store (<https://cds.climate.copernicus.eu/cdsapp#!/dataset/reanalysis-era5-pressure-levels-monthly-means/>).
- ERSSTv5 can be obtained via NOAA's NCEI website at [https://www.ncei.noaa.gov/access/metadata/landing-page/bin/iso?id=gov.noaa.ncdc:  
 1193 C00927](https://www.ncei.noaa.gov/access/metadata/landing-page/bin/iso?id=gov.noaa.ncdc:C00927)

1194

1195

1196

- CMAP Precipitation data provided by the NOAA/OAR/ESRL PSL, Boulder, Colorado, USA, from their Web site at <https://psl.noaa.gov/data/gridded/data.cmap.html>. 1197  
1198  
1199
- The Oceanic Niño Index is available via NOAA's Climate Prediction Center: [https://www.cpc.ncep.noaa.gov/products/analysis\\_monitoring/ensostuff/detrend.nino34.ascii.txt](https://www.cpc.ncep.noaa.gov/products/analysis_monitoring/ensostuff/detrend.nino34.ascii.txt). 1200  
1201  
1202
- The Oceanic Niño Index is available via NOAA's Climate Prediction Center: [https://www.cpc.ncep.noaa.gov/products/analysis\\_monitoring/ensostuff/detrend.nino34.ascii.txt](https://www.cpc.ncep.noaa.gov/products/analysis_monitoring/ensostuff/detrend.nino34.ascii.txt). 1203  
1204  
1205
- The Dipole Mode Index is available via Global Climate Observing System Working Group on Surface Pressure: [https://psl.noaa.gov/gcos\\_wgsp/Timeseries/Data/dmi.had.long.data](https://psl.noaa.gov/gcos_wgsp/Timeseries/Data/dmi.had.long.data) 1206  
1207  
1208  
1209

## Code availability

A version-controlled repository of the code used to create this analysis, including the code used to download the data can be found at <https://github.com/eliocamp/shceof>.

## Authors' contributions

E.C. made the data curation, formal analysis and prepared all the figures. E.C. and L.D. wrote the main manuscript text. All authors reviewed the manuscript.

## A Extra figures

**code-availability**  
1211  
1212  
1213  
1214  
1215  
1216  
1217  
1218  
1219  
1220  
1221  
1222  
1223  
1224  
1225  
1226  
1227  
1228  
1229  
1230  
1231  
1232  
1233  
1234  
1235  
1236  
1237  
1238  
1239  
1240  
1241  
1242

**authors-contributions**

**extra-figures**

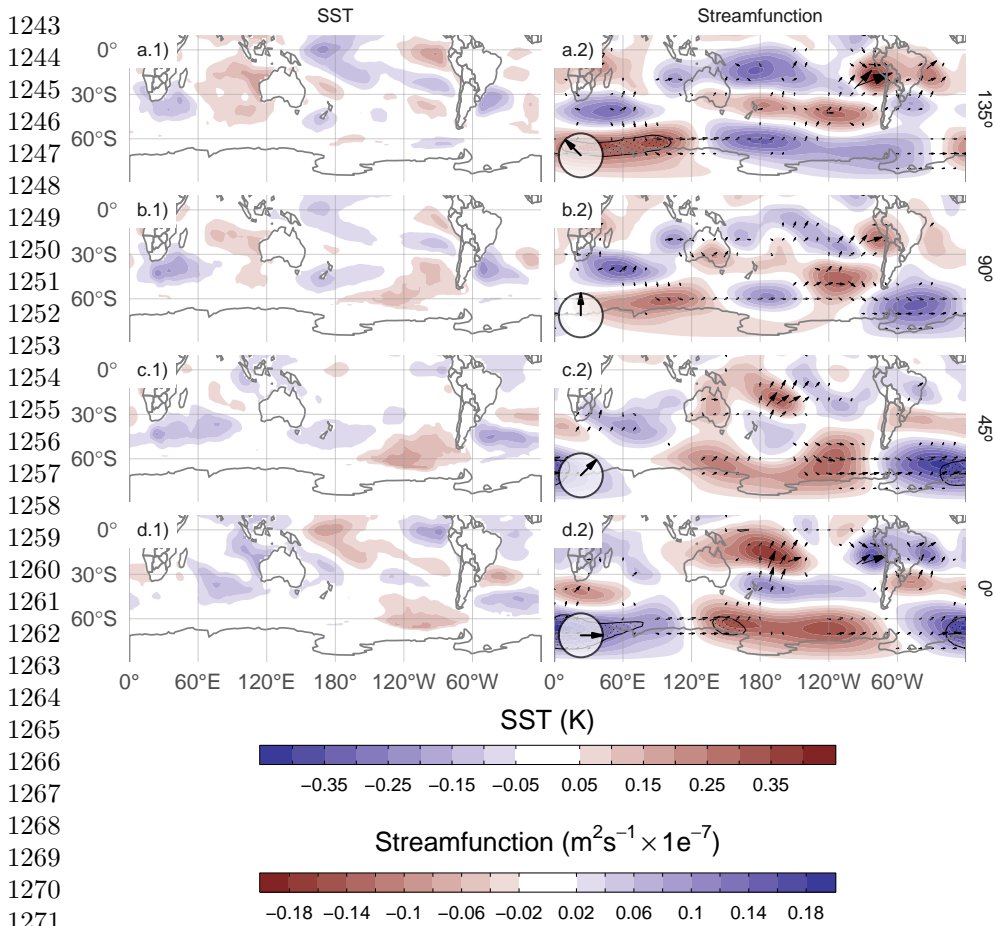
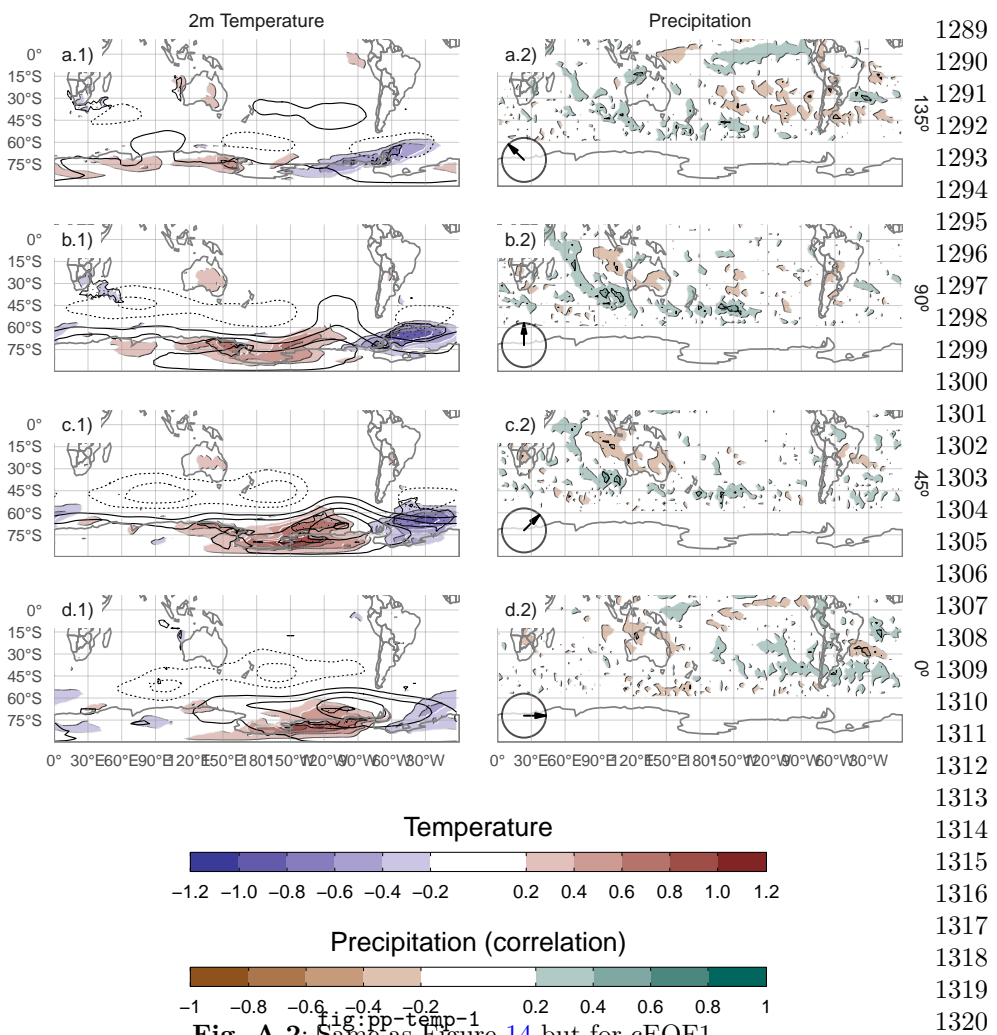


**Fig. A.1:** Same as Figure 11 but for cEOF1.

fig:sst-psi-1

## References

- Adams JC, Swartztrauber PN, Sweet R (1999) FISHPACK, a package of Fortran subprograms for the solution of separable elliptic partial differential equations. <https://www2.cisl.ucar.edu/resources/legacy/fishpack>
- Albers S, Campitelli E (2020) Rsoi: Import Various Northern and Southern Hemisphere Climate Indices
- Allaire JJ, Xie [aut Y, cre, et al (2020) Rmarkdown: Dynamic Documents for R
- Baldwin MP, Thompson DWJ (2009) A critical comparison of stratosphere–troposphere coupling indices. Quarterly Journal of the Royal Meteorological Society 135(644):1661–1672. <https://doi.org/10.1002/qj.479>



Bamston AG, Chelliah M, Goldenberg SB (1997) Documentation of a highly ENSO-related sst region in the equatorial pacific: Research note. *Atmosphere-Ocean* 35(3):367–383. <https://doi.org/10.1080/07055900.1997.9649597>

Bell B, Hersbach H, Berrisford P, et al (2020) ERA5 monthly averaged data on pressure levels from 1950 to 1978 (preliminary version). Copernicus Climate Change Service (C3S) Climate Data Store (CDS) (Accessed on <26-08-2021>), <https://cds.climate.copernicus.eu/cdsapp#!/dataset/reanalysis-era5-pressure-levels-monthly-means-preliminary-back-extension?tab=overview>

1289  
1290  
1291  
1292  
1293  
1294  
1295  
1296  
1297  
1298  
1299  
1300  
1301  
1302  
1303  
1304  
1305  
1306  
1307  
1308  
1309  
1310  
1311  
1312  
1313  
1314  
1315  
1316  
1317  
1318  
1319  
1320  
1321  
1322  
1323  
1324  
1325  
1326  
1327  
1328  
1329  
1330  
1331  
1332  
1333  
1334

- 1335 Benjamini Y, Hochberg Y (1995) Controlling the False Discovery Rate: A  
1336 Practical and Powerful Approach to Multiple Testing. *Journal of the Royal  
1337 Statistical Society: Series B (Methodological)* 57(1):289–300. <https://doi.org/10.1111/j.2517-6161.1995.tb02031.x>
- 1339
- 1340 Cai W, Watterson IG (2002) Modes of Interannual Variability of the Southern  
1341 Hemisphere Circulation Simulated by the CSIRO Climate Model. *Journal  
1342 of Climate* 15(10):1159–1174. [https://doi.org/10.1175/1520-0442\(2002\)  
015<1159:MOIVOT>2.0.CO;2](https://doi.org/10.1175/1520-0442(2002)<br/>015<1159:MOIVOT>2.0.CO;2)
- 1344
- 1345 Cai W, van Rensch P, Cowan T, et al (2011a) Teleconnection Pathways  
1346 of ENSO and the IOD and the Mechanisms for Impacts on Australian  
1347 Rainfall. *Journal of Climate* 24(15):3910–3923. [https://doi.org/10.1175/  
2011JCLI4129.1](https://doi.org/10.1175/<br/>2011JCLI4129.1)
- 1349
- 1350 Cai W, Sullivan A, Cowan T (2011b) Interactions of ENSO, the IOD, and  
1351 the SAM in CMIP3 Models. *Journal of Climate* 24(6):1688–1704. [https://doi.org/10.1175/  
2010JCLI3744.1](https://doi.org/10.1175/<br/>2010JCLI3744.1)
- 1353
- 1354 Cai W, McPhaden MJ, Grimm AM, et al (2020) Climate impacts of the  
1355 El Niño–Southern Oscillation on South America. *Nature Reviews Earth &  
1356 Environment* 1(4):215–231. <https://doi.org/10.1038/s43017-020-0040-3>
- 1357 Campitelli E (2020) metR: Tools for Easier Analysis of Meteorological Fields  
1358
- 1359 Campitelli E, Díaz L, Vera C (2022a) Data for "Revisiting the Austral Spring  
1360 Extratropical Southern Hemisphere zonally asymmetric circulation using  
1361 complex Empirical Orthogonal Functions". [https://doi.org/10.5281/zenodo.  
6612324](https://doi.org/10.5281/zenodo.<br/>6612324)
- 1363
- 1364 Campitelli E, Díaz LB, Vera C (2022b) Assessment of zonally symmetric  
1365 and asymmetric components of the Southern Annular Mode using a  
1366 novel approach. *Climate Dynamics* 58(1):161–178. [https://doi.org/10.1007/  
s00382-021-05896-5](https://doi.org/10.1007/<br/>s00382-021-05896-5)
- 1368
- 1369 Carvalho LMV, Jones C, Ambrizzi T (2005) Opposite Phases of the Antarctic  
1370 Oscillation and Relationships with Intraseasonal to Interannual Activity in  
1371 the Tropics during the Austral Summer. *Journal of Climate* 18(5):702–718.  
1372 <https://doi.org/10.1175/JCLI-3284.1>
- 1373
- 1374 Cazes-Boezio G, Robertson AW, Mechoso CR (2003) Seasonal Dependence of  
1375 ENSO Teleconnections over South America and Relationships with Precipi-  
1376 tation in Uruguay. *Journal of Climate* 16(8):1159–1176. [https://doi.org/10.  
1175/1520-0442\(2003\)16<1159:SDOETO>2.0.CO;2](https://doi.org/10.<br/>1175/1520-0442(2003)16<1159:SDOETO>2.0.CO;2)
- 1377
- 1378 Ciasto LM, Simpkins GR, England MH (2015) Teleconnections between Tropi-  
1379 cal Pacific SST Anomalies and Extratropical Southern Hemisphere Climate.  
1380

- Journal of Climate 28(1):56–65. <https://doi.org/10.1175/JCLI-D-14-00438.1> 1381  
1382  
1383  
1384  
1385  
1386  
1387  
1388  
1389  
1390  
1391  
1392  
1393  
1394  
1395  
1396  
1397  
1398  
1399  
1400  
1401  
1402  
1403  
1404  
1405  
1406  
1407  
1408  
1409  
1410  
1411  
1412  
1413  
1414  
1415  
1416  
1417  
1418  
1419  
1420  
1421  
1422  
1423  
1424  
1425  
1426
- Dowle M, Srinivasan A (2020) Data.table: Extension of 'data.frame'
- Fogt RL, Marshall GJ (2020) The Southern Annular Mode: Variability, trends, and climate impacts across the Southern Hemisphere. WIREs Climate Change 11(4):e652. <https://doi.org/10.1002/wcc.652>
- Gelbrecht M, Boers N, Kurths J (2018) Phase coherence between precipitation in South America and Rossby waves. Science Advances 4(12):eaau3191. <https://doi.org/10.1126/sciadv.aau3191>
- Gong D, Wang S (1999) Definition of Antarctic Oscillation index. Geophysical Research Letters 26(4):459–462. <https://doi.org/10.1029/1999GL900003>
- Goyal R, Jucker M, Gupta AS, et al (2022) A new zonal wave 3 index for the Southern Hemisphere. Journal of Climate -1(aop):1–25
- Grytsai A (2011) Planetary wave peculiarities in Antarctic ozone distribution during 1979–2008. International Journal of Remote Sensing 32(11):3139–3151. <https://doi.org/10.1080/01431161.2010.541518>
- Hartmann DL, Garcia RR (1979) A Mechanistic Model of Ozone Transport by Planetary Waves in the Stratosphere. Journal of the Atmospheric Sciences 36(2):350–364. [https://doi.org/10.1175/1520-0469\(1979\)036<0350:AMMOOT>2.0.CO;2](https://doi.org/10.1175/1520-0469(1979)036<0350:AMMOOT>2.0.CO;2)
- Hersbach H, Bell B, Berrisford P, et al (2019) ERA5 monthly averaged data on pressure levels from 1979 to present. Copernicus Climate Change Service (C3S) Climate Data Store (CDS) (Accessed on <07-09-2021>). <https://doi.org/10.24381/cds.6860a573>
- Hobbs WR, Raphael MN (2010) Characterizing the zonally asymmetric component of the SH circulation. Climate Dynamics 35(5):859–873. <https://doi.org/10.1007/s00382-009-0663-z>
- Horel JD (1984) Complex Principal Component Analysis: Theory and Examples. Journal of Applied Meteorology and Climatology 23(12):1660–1673. [https://doi.org/10.1175/1520-0450\(1984\)023<1660:CPCATA>2.0.CO;2](https://doi.org/10.1175/1520-0450(1984)023<1660:CPCATA>2.0.CO;2)
- Hoskins BJ, Hodges KI (2005) A New Perspective on Southern Hemisphere Storm Tracks. Journal of Climate 18(20):4108–4129. <https://doi.org/10.1175/JCLI3570.1>
- Huang B, Thorne PW, Banzon VF, et al (2017) Extended Reconstructed Sea Surface Temperature, Version 5 (ERSSTv5): Upgrades, Validations, and

32 *SH zonally asymmetric circulation with cEOF*

- 1427 Intercomparisons. *Journal of Climate* 30(20):8179–8205. <https://doi.org/10.1175/JCLI-D-16-0836.1>
- 1428
- 1429
- 1430 Hufkens K (2020) Ecmwfr: Programmatic interface to the two European  
1431 Centre for Medium-Range Weather Forecasts API services
- 1432
- 1433 Irving D, Simmonds I (2015) A Novel Approach to Diagnosing Southern  
1434 Hemisphere Planetary Wave Activity and Its Influence on Regional Climate  
1435 Variability. *Journal of Climate* 28(23):9041–9057. <https://doi.org/10.1175/JCLI-D-15-0287.1>
- 1436
- 1437 Irving D, Simmonds I (2016) A New Method for Identifying the Pacific–South  
1438 American Pattern and Its Influence on Regional Climate Variability. *Journal*  
1439 of Climate 29(17):6109–6125. <https://doi.org/10.1175/JCLI-D-15-0843.1>
- 1440
- 1441 Kao HY, Yu JY (2009) Contrasting Eastern-Pacific and Central-Pacific  
1442 Types of ENSO. *Journal of Climate* 22(3):615–632. <https://doi.org/10.1175/2008JCLI2309.1>
- 1442
- 1443
- 1444
- 1445 Katz RW, Brown BG (1991) The problem of multiplicity in research on  
1446 teleconnections. *International Journal of Climatology* 11(5):505–513. <https://doi.org/10.1002/joc.3370110504>
- 1446
- 1447
- 1448
- 1449 Krokhin VV, Luxemburg WMJ (2007) Temperatures and precipitation totals  
1450 over the Russian Far East and Eastern Siberia: Long-term variability and  
1451 its links to teleconnection indices. *Hydrology and Earth System Sciences*  
1452 11(6):1831–1841. <https://doi.org/10.5194/hess-11-1831-2007>
- 1453
- 1454 L'Heureux ML, Thompson DWJ (2006) Observed Relationships between the  
1455 El Niño–Southern Oscillation and the Extratropical Zonal-Mean Circula-  
1456 tion. *Journal of Climate* 19(2):276–287. <https://doi.org/10.1175/JCLI3617.1>
- 1456
- 1457
- 1458
- 1459 Lim EP, Hendon HH, Thompson DWJ (2018) Seasonal Evolution of  
1460 Stratosphere-Troposphere Coupling in the Southern Hemisphere and Impli-  
1461 cations for the Predictability of Surface Climate. *Journal of Geophysical*  
1462 *Research: Atmospheres* 123(21):12,002–12,016. <https://doi.org/10.1029/2018JD029321>
- 1463
- 1464 Mo KC (2000) Relationships between Low-Frequency Variability in the  
1465 Southern Hemisphere and Sea Surface Temperature Anomalies. *Jour-*  
1466 *nal of Climate* 13(20):3599–3610. [https://doi.org/10.1175/1520-0442\(2000\)013<3599:RBLFVI>2.0.CO;2](https://doi.org/10.1175/1520-0442(2000)013<3599:RBLFVI>2.0.CO;2)
- 1467
- 1468
- 1469 Mo KC, Paegle JN (2001) The Pacific–South American modes and their  
1470 downstream effects. *International Journal of Climatology* 21(10):1211–1229.  
1471 <https://doi.org/10.1002/joc.685>
- 1472

- Nuncio M, Yuan X (2015) The Influence of the Indian Ocean Dipole on Antarctic Sea Ice. *Journal of Climate* 28(7):2682–2690. <https://doi.org/10.1175/JCLI-D-14-00390.1> 1473  
 1474  
 1475  
 1476  
 1477  
 1478  
 1479  
 1480  
 1481  
 1482  
 1483  
 1484  
 1485  
 1486  
 1487  
 1488  
 1489  
 1490  
 1491  
 1492  
 1493  
 1494  
 1495  
 1496  
 1497  
 1498  
 1499  
 1500  
 1501  
 1502  
 1503  
 1504  
 1505  
 1506  
 1507  
 1508  
 1509  
 1510  
 1511  
 1512  
 1513  
 1514  
 1515  
 1516  
 1517  
 1518
- Pezza AB, Rashid HA, Simmonds I (2012) Climate links and recent extremes in antarctic sea ice, high-latitude cyclones, Southern Annular Mode and ENSO. *Climate Dynamics* 38(1):57–73. <https://doi.org/10.1007/s00382-011-1044-y>
- Plumb RA (1985) On the Three-Dimensional Propagation of Stationary Waves. *Journal of the Atmospheric Sciences* 42(3):217–229. [https://doi.org/10.1175/1520-0469\(1985\)042<0217:OTTDPO>2.0.CO;2](https://doi.org/10.1175/1520-0469(1985)042<0217:OTTDPO>2.0.CO;2)
- R Core Team (2020) R: A Language and Environment for Statistical Computing. R Foundation for Statistical Computing, Vienna, Austria
- Raphael M (2003) Recent, Large-Scale Changes in the Extratropical Southern Hemisphere Atmospheric Circulation. *Journal of Climate* 16(17):2915–2924. [https://doi.org/10.1175/1520-0442\(2003\)016<2915:RLCITE>2.0.CO;2](https://doi.org/10.1175/1520-0442(2003)016<2915:RLCITE>2.0.CO;2)
- Raphael MN (2004) A zonal wave 3 index for the Southern Hemisphere. *Geophysical Research Letters* 31(23). <https://doi.org/10.1029/2004GL020365>
- Raphael MN (2007) The influence of atmospheric zonal wave three on Antarctic sea ice variability. *Journal of Geophysical Research: Atmospheres* 112(D12). <https://doi.org/10.1029/2006JD007852>
- Saji NH, Yamagata T (2003) Possible impacts of Indian Ocean Dipole mode events on global climate. *Climate Research* 25(2):151–169. <https://doi.org/10.3354/cr025151>
- Saji NH, Goswami BN, Vinayachandran PN, et al (1999) A dipole mode in the tropical Indian Ocean. *Nature* 401(6751):360–363. <https://doi.org/10.1038/43854>
- Smith AK (1995) Numerical simulation of global variations of temperature, ozone, and trace species in the stratosphere. *Journal of Geophysical Research: Atmospheres* 100(D1):1253–1269. <https://doi.org/10.1029/94JD02395>
- Trenberth KE (1980) Planetary Waves at 500 mb in the Southern Hemisphere. *Monthly Weather Review* 108(9):1378–1389. [https://doi.org/10.1175/1520-0493\(1980\)108<1378:PWAMIT>2.0.CO;2](https://doi.org/10.1175/1520-0493(1980)108<1378:PWAMIT>2.0.CO;2)
- Trenberth KF, Mo KC (1985) Blocking in the Southern Hemisphere. *Monthly Weather Review* 113(1):3–21. [https://doi.org/10.1175/1520-0493\(1985\)113<0003:BITSH>2.0.CO;2](https://doi.org/10.1175/1520-0493(1985)113<0003:BITSH>2.0.CO;2)

34 *SH zonally asymmetric circulation with cEOF*

- 1519 Turner J, Hosking JS, Bracegirdle TJ, et al (2017) Variability and trends in  
1520 the Southern Hemisphere high latitude, quasi-stationary planetary waves.  
1521 International Journal of Climatology 37(5):2325–2336. <https://doi.org/10.1002/joc.4848>
- 1523
- 1524 van Loon H, Jenne RL (1972) The zonal harmonic standing waves in the south-  
1525 ern hemisphere. Journal of Geophysical Research 77(6):992–1003. <https://doi.org/10.1029/JC077i006p00992>
- 1527
- 1528 Walker SGT (1914) Correlation in Seasonal Variations of Weather, III: On the  
1529 Criterion for the Reality of Relationships Or Periodicities. Meteorological  
1530 Office
- 1531
- 1532 Wickham H (2009) Ggplot2: Elegant Graphics for Data Analysis. Use R!,  
1533 Springer-Verlag, New York, <https://doi.org/10.1007/978-0-387-98141-3>
- 1534
- 1535 Wilks D (2011) Statistical Methods in the Atmospheric Sciences, vol 100.  
1536 Elsevier, <https://doi.org/10.1016/B978-0-12-385022-5.00022-1>
- 1537
- 1538 Wilks DS (2016) “The Stippling Shows Statistically Significant Grid Points”:  
1539 How Research Results are Routinely Overstated and Overinterpreted, and  
1540 What to Do about It. Bulletin of the American Meteorological Society  
1541 97(12):2263–2273. <https://doi.org/10.1175/BAMS-D-15-00267.1>
- 1542
- 1543 Wirth V (1993) Quasi-stationary planetary waves in total ozone and their  
1544 correlation with lower stratospheric temperature. Journal of Geophys-  
1545 ical Research: Atmospheres 98(D5):8873–8882. <https://doi.org/10.1029/92JD02820>
- 1546
- 1547 Xie P, Arkin PA (1997) Global Precipitation: A 17-Year Monthly Analysis  
1548 Based on Gauge Observations, Satellite Estimates, and Numerical Model  
1549 Outputs. Bull Amer Meteor Soc 78 (Accessed on <26-08-2021>)(11):2539–  
1550 2558. [https://doi.org/10.1175/1520-0477\(1997\)078<2539:GPAYMA>2.0.CO;2](https://doi.org/10.1175/1520-0477(1997)078<2539:GPAYMA>2.0.CO;2)
- 1552
- 1553 Xie Y (2015) Dynamic Documents with R and Knitr, 2nd edn. Chapman and  
1554 Hall/CRC, Boca Raton, Florida
- 1555
- 1556
- 1557
- 1558
- 1559
- 1560
- 1561
- 1562
- 1563
- 1564